Submitted to PASP July 16, 2015.

Spatial and Temporal Stability of Airglow Measured in the Meinel Band Window at 1191.3 nm

Hien T. Nguyen[1,2*], Michael Zemcov[2,1], John Battle[2], James J. Bock[2,1], Viktor Hristov[2], Philip Korngut[1,2], and Andrew Meek[2]

[1] *Jet Propulsion Laboratory (JPL), National Aeronautics and Space Administration (NASA), Pasadena, CA 91109, USA*

[2] *Department of Physics, Mathematics and Astronomy, California Institute of Technology, Pasadena, CA 91125, USA*

[*] htnguyen@jpl.nasa.gov

ABSTRACT

We report on the temporal and spatial fluctuations in the atmospheric brightness in the narrow band between Meinel emission lines at 1191.3 nm using a $\lambda/\Delta\lambda = 320$ near-infrared instrument. We present the instrument design and implementation, followed by a detailed analysis of data taken over the course of a night from Table Mountain Observatory. The absolute sky brightness at this wavelength is found to be 5330 ± 30 nW m^{-2} sr^{-1}, consistent with previous measurements of the inter-band airglow at these wavelengths. This amplitude is larger than simple models of the continuum component of the airglow emission at these wavelengths, confirming that an extra emissive or scattering component is required to explain the observations. We perform a detailed investigation of the noise properties of the data and find no evidence for a noise component associated with temporal instability in the inter-line continuum. This result demonstrates that in several hours of ~ 100 s integrations the noise performance of the instrument does not appear to significantly degrade from expectations, giving a proof of concept that near-IR line intensity mapping may be feasible from ground-based sites.

Subject headings: atmospheric effects – site testing – techniques: imaging spectroscopy

1. Introduction

Recent results (e.g. Kashlinsky et al. 2005, Matsumoto et al. 2011, Zemcov et al. 2013a) suggest there are large-angular scale fluctuations in the near-infrared (IR) extragalactic background light (EBL) larger than models of galaxy clustering predict (Helgason et al. 2012). This component

appears to reach a maximum brightness between 1 and 2 μm, wavelengths at which terrestrial airglow is very bright (Leinert et al. 1998). As a result, the aforementioned measurements of the large-angular emission have only been performed from space-based platforms in broad photometric bands. Due to the complexity of space-based measurements, such observations are expensive. As a result, the ability to make ground-based observations of this component would significantly expedite progress.

Airglow in the near-IR prohibits measurement of large-angular scale structure in broad bands from the ground. In the range $800 < \lambda < 2000$ nm, the predominant mechanism responsible for airglow is emission from reactions between O_3 and H in the upper atmosphere (Le Texier et al. 1987), called Meinel emission (Meinel 1950). Because of the properties of oxygen mixing in the atmosphere, airglow is produced in a discrete layer between 75 and 100 km (von Savigny et al. 2012), so observations made from different ground-based sites should see similar brightness. The Meinel spectrum exhibits a large number of narrow lines, which averaged over wide bands lead to backgrounds of $\sim 15\,\mathrm{mag_{AB}\ arcsec^{-2}}$. However, in $\lambda/\Delta\lambda \sim 100$ windows between the lines the sky is stable and approaches a surface brightness of $\sim 20\,\mathrm{mag_{AB}\ arcsec^{-2}}$ (Sullivan & Simcoe 2012). If the OH line positions are sufficiently stable, it should be possible to perform imaging measurements in the continuum windows between them.

In this work, we investigate the stability of the large scale spatial structure measured in a $\lambda/\Delta\lambda = 320$ band centered at 1191.3 nm. This wavelength is selected to lie between emission lines in the atmosphere, as shown in Figure 1. We use a custom-built instrument, the Lyman Alpha Mapping Prototype (LAMP), to measure the atmospheric stability in the 1191.3 nm window in a $1^\circ.2 \times 1^\circ.2$ field from Table Mountain Observatory, California. To characterize the stability of the atmosphere, we investigate the total sky brightness, the noise in the instrument, and the spatial power spectrum of the noise. The LAMP instrument is presented in Section 2, the observations and data analysis are presented in Sections 3 and 4, respectively, and various results are shown in Section 5. We conclude with a discussion of the implications of these measurements in Section 6.

2. The Instrument

LAMP comprises of a modest commercial telescope coupled to a cryogenic camera that images on a HAWAII-1 infrared detector array. This section describes (i) the LAMP instrument, including its optics, mechanical assembly and readout electronics, and (ii) the instrument's expected sensitivity to fluctuations. In addition to customized components, LAMP makes use of existing flight spares and laboratory testing apparatus for the imaging camera of CIBER (Cosmic Infrared Background Experiment; Bock et al. 2013, Zemcov et al. 2013b).

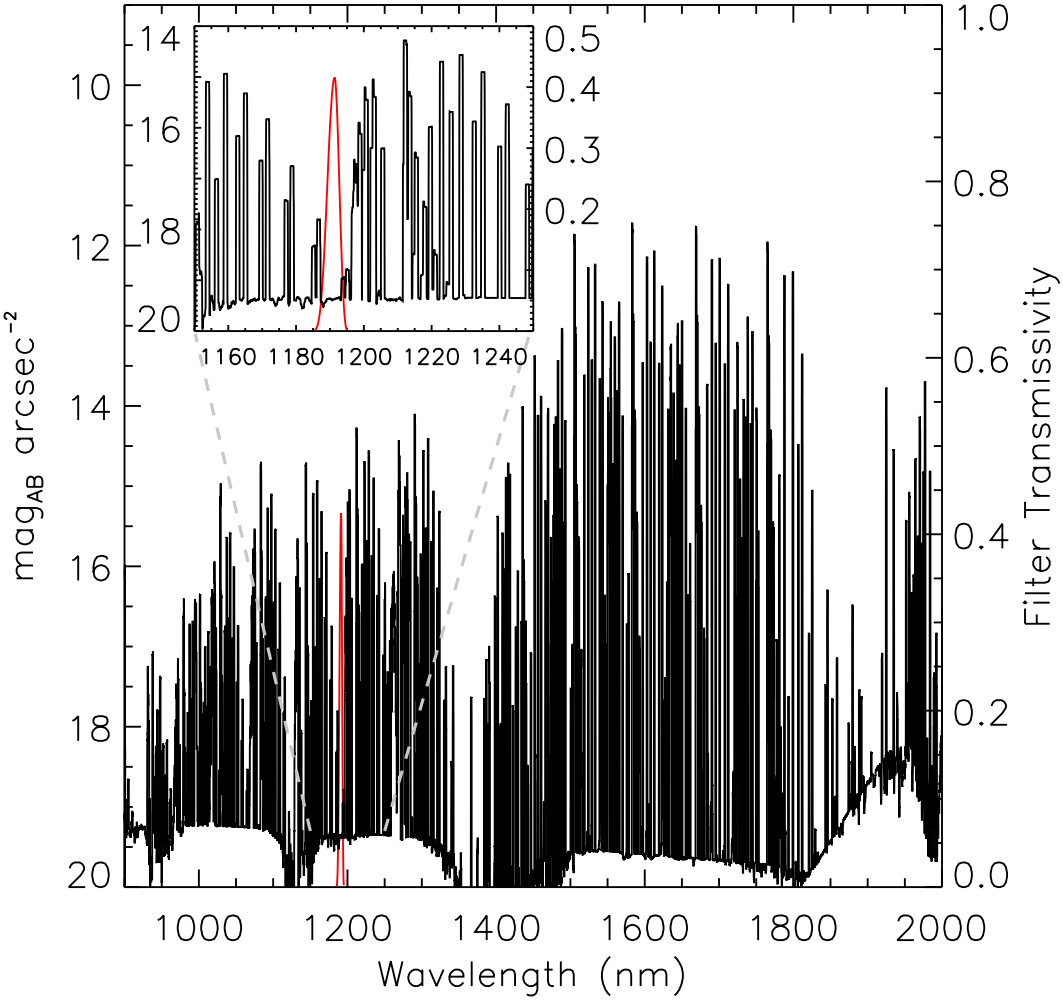

Fig. 1.— The predicted surface brightness of the atmosphere between 0.9 and 2.0 μm. The atmospheric emission spectrum is derived from the Gemini Observatory sky background model (black line). This model is generated using the sky transmission files generated by ATRAN (Lord 1992) scaled to a 273 K blackbody. We assume 5 mm of precipitable water vapor in this calculation, which is consistent with the typical value above Table Mountain during clear weather (Leblanc et al. 2011). An OH emission spectrum, a set of O_2 lines near 1.3 μm, and the dark sky continuum (including solar-spectrum Zodiacal light) are summed to the thermal spectrum to account for those components. This model reproduces measurements like those of Sullivan & Simcoe (2012) averaged over broad bands. The LAMP bandpass is situated in a narrow minimum in the emission spectrum (red line; see Section 2.1.1), reducing the effect of variation in the OH lines on the overall brightness.

2.1. Instrument Description

2.1.1. The Optics

LAMP uses a commercial 10″ Newtonian telescope[1] coupled to a liquid Nitrogen (LN_2) cooled camera operating at 80 K. Figure 2 contains schematics of both the telescope and optical chain. Light enters the camera cryostat[2] through a $d = 60$ mm optical window[3] and is imaged by three aspheric lenses[4] optimized to mitigate coma from the telescope in order to achieve the full $1^\circ.2 \times 1^\circ.2$ field of view (FOV). The light is then filtered by a configurable optical filter stack, and finally is detected by the near-IR detector array. The window and lenses are all anti-reflection (AR) coated; the transmissivity of the various optical components at 1190 nm determined either during manufacture or under test in the laboratory are given in Table 1.

Table 1: LAMP optical efficiency budget at 1190 nm.

Component	η
Mirrors	0.90
Window	0.95
Optics	0.89
Optics Total	0.76
Science 1191.3 nm Filter	0.75
Blocking Filter 1	0.76
Blocking Filter 2	0.72
Filter Total	0.41
Total Optical Efficiency	0.31

The filter stack is designed to accomodate up to 3 optical filters in series. In the configuration used for this measurement, we installed both the narrow band 1191.3 nm filter and two blocking filters to reduce the out of band transmissivity of the system[5]. This stringent blocking of the out of band photons is crucial, motivated by the fact that the airglow has a specific surface brightness of $I_\lambda \sim 5000$ nW m^{-2} sr^{-1} μm^{-1} in the near IR, so that filter leaks could easily dominate the small in-band signal in this measurement. The filters are installed with the narrow band filter closest to the camera optics parallel to the detector surface, and the two blocking filters closest to the detector are tipped by 4° to mitigate optical ghosting from reflections from the detector surface. In Figure 3 we show the theoretical spectral bandpass for the instrument, and measurements of

[1]Manufactured by Parks Optical Inc., http://www.parksoptical.com.

[2]Manufactured by IR Labs Part Number HDL-8 http://http://www.infraredlaboratories.com.

[3]Manufactured by Omega Optical Inc., http://www.omgeafilters.com.

[4]Manufactured by The Genesia Corporation, http://www.genesia.co.jp.

[5]Manufactured by Chroma Technology Corp. to customized specifications, http://www.chroma.com

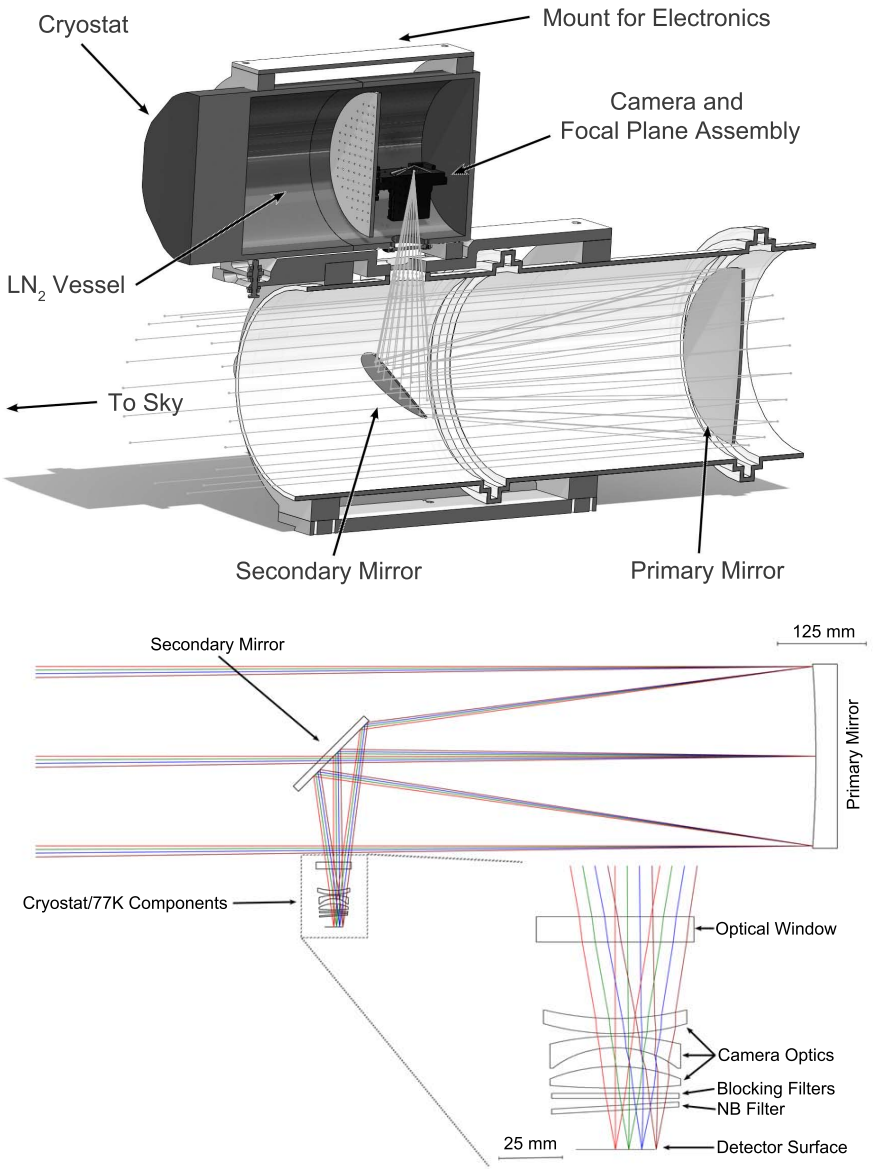

Fig. 2.— Schematic views of the LAMP instrument and optical chain. The upper panel shows a sectional view of a solid model of the LAMP system, showing the Newtonian telescope and cryostat including the camera optics and HAWAII-1 detector array. A narrow-band interference filter installed between the camera and detector is used to observe between the OH airglow lines emitted by the Earths upper atmosphere. The entire assembly is mounted on the top of TMF 24″ telescope (see Figure 4). The lower panel shows a schematic of the LAMP optical chain highlighting the Newtonian telescope comprising a spherical primary and flat secondary, coupled to a wide field camera. The optical ray trace shows the principal ray (red) and rays every $d\theta = +0.33°$ (green, blue, brown). The negative $d\theta$ rays are suppressed but are symmetric to the positive rays. The camera comprises 3 powered lenses and facility for up to 3 optical filters in series. The filters are tipped with respect to one another to eliminate reflections from the detector surface which would cause optical ghosting. The optical efficiencies of the various components are given in Table 1.

the bandpass made in the laboratory. We place upper limits on the out of band blocking using laboratory measurements, and find that for $0.8 < \lambda < 2.5\,\mu$m the out of band rejection is $> 10^4$. This gives an upper limit on the out of band contribution to the photocurrent of $< 1.5\,\%$, integrating over the wavelength range to which our HgCdTe detectors are responsive.

2.1.2. Mechanical and Cryogenic Systems

The telescope tube is firmly supported by a pair of circular clamps made of cast-iron. The top and bottom of these clamps are mounted on metal interfaces. The top interface is used to attach a small cryostat that houses the camera lens and its detector array. The cryostat holds approximately 5 liters of LN_2, which lasts for 48 hours between service. The cryogen passively cools both the camera lenses and detectors to < 80 K. The entire instrument assembly, totaling a weight of 200 lbs, is mounted on an existing 60 cm telescope (at Table Mountain Observatory), to benefit from the use of the larger telescope's pointing and tracking.

The LAMP system uses a focal plane assembly (FPA) from the CIBER instrument, comprising nested light-tight housings for the detectors and associated cryogenic electronics allowing active thermal control of the detector. The FPA unit is described in detail in Zemcov et al. (2013b). The FPA unit is attached to the camera at a distance determined to bring the telescope in focus in the laboratory.

2.1.3. Detector and Readout Electronics

LAMP uses the same 1024×1024 HAWAII-1[6] HgCdTe detector array as is used by the CIBER instrument[7]. A detailed presentation of the properties of this detector can be found in Bock et al. (2013). LAMP also uses the same readout chain as used for CIBER, slightly modified to operate with a single channel. The electronic system is presented in Section 4 of Zemcov et al. (2013b); for LAMP the system is used in 'Serial Mode'. Because of their heritage of use in sounding rockets where there are concerns about targeting computer trigger loss, the electronics are configured to have a maximum of 70 integrations before resetting the array. This limits the maximum data set length obtainable with these electronics to < 110 s.

---

[6]Manufactured by Teledyne Scientific & Imaging LLC, http://www.teledyne-si.com.

[7]Serial number Hawaii-211.

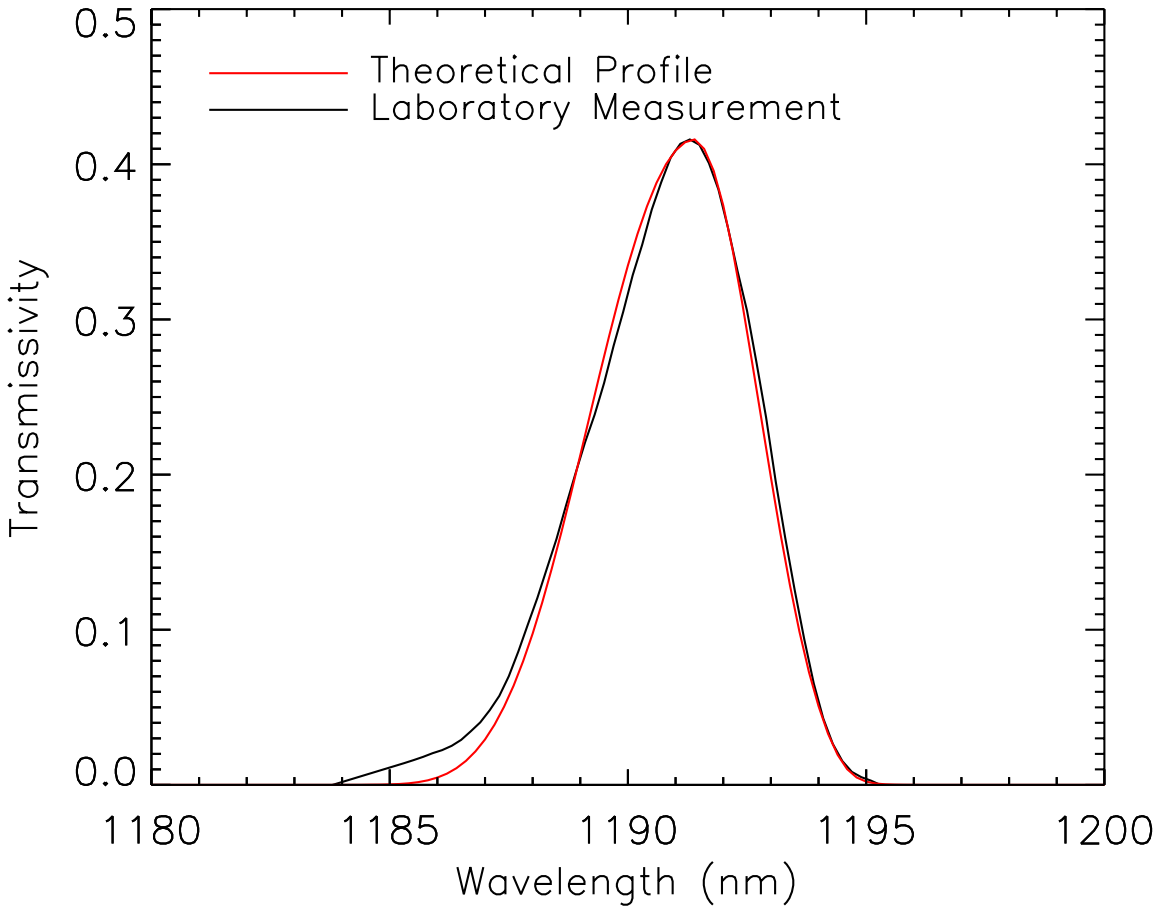

Fig. 3.— The transmissivity of the total LAMP filter stack, comprising a bandpass filter and two tilted out-of-band blocking filters. The measured transmissivity is determined in the laboratory at 77 K using a monochromator with a $\delta\lambda = 1.8$ nm dispersion, causing a broadening of the measurement compared to the intrinsic width of the filter. The theoretical transmissivity curve is calculated from the $\theta = 0°$ angle of incidence filter transmissivity provided by the filter manufacturer in two steps. First, the transmissivity curve is convolved with the square spectral function of the monochromator. Secondly, the transmissivity short-ward of the filter peak is convolved with a "blue broadening" function following $\lambda = \lambda_0 \cos\theta$ (Korngut et al. 2013), where λ_0 is the response at normal angle of incidence and the optics are $f/3.4$ through the bandpass filter. The FWHM of this filter configuration as measured is 4.1 nm, but after removing the effect of the monochromator spectral function the intrinsic width of the filter stack is determined to be 3.7 nm.

2.2. Theoretical Sensitivity

We can calculate the theoretical sensitivity of LAMP given known instrument parameters and the approximate brightness of the sky. The equation relating the photo current at the detector $i_{\rm phot}$ to the brightness of a beam-filling astronomical source λI_λ is:

$$i_{\rm phot} \simeq \lambda I_\lambda \left(\frac{\eta A \Omega}{h\nu} \frac{\Delta\lambda}{\lambda} \right), \tag{1}$$

where η is the system efficiency, A is the area of the aperture, Ω is the angular size of a pixel, $\Delta\lambda/\lambda$ is the fractional filter width, and $h\nu$ is the energy of the photons in the LAMP band (see the Appendix to Bock et al. 2013 for a discussion). The photometric surface brightness calibration $\mathcal{C} = \lambda I_\lambda / i_{\rm phot}$ is given by the term in brackets on the right hand side of Equation 1, and relates the sky brightness in nW m^{-2} sr^{-1} to the measured photocurrent in e$^-$s^{-1}. The instrument parameters we have determined for LAMP are summarized in Table 2. Based on these values, we calculate $\mathcal{C} = 5.65 \times 10^4$ nW m^{-2} sr^{-1}/e^- s^{-1}.

Table 2: LAMP Instrument Parameters

Parameter	Value	Units
Operating Wavelength	1191.3 nm	nm
Filter Width	3.7	nm
F#	3.4	
Focal Length	865.9	mm
Clear Aperture	390	cm^2
Pixel Size	4.3×4.3	arcsec
Field of View	1.2×1.2	deg
Optical Efficiency	0.31	
Array QE	0.52	$*$
Total Efficiency	0.16	
Array Format	1024^2	
Pixel Pitch	18	μm
Read Noise (CDS)	10	e^-
Frame Interval	1.78	s
Theoretical Surface Brightness Calibration	5.65×10^4	nW m^{-2} sr^{-1}/e$^-$s^{-1}

$*$ Array QE is estimated from QE measured at 2.2 μm and scaled based on the response of a typical Hawaii-1.

In this analysis, we fit a linear model to constant frame interval reads of the detector array to estimate the photocurrent in a given integration. The instrument read noise $\sigma_{\rm read}$ for this estimator is given by:

$$\sigma^2_{\rm read} = \frac{12 N \sigma^2_{\rm CDS}}{(N^2-1) T^2_{\rm int}} \tag{2}$$

where N is the number of frames in an integration, $\sigma_{\rm CDS}$ is the single frame read noise estimated using the root mean squared variation in a correlated-double-sample, and $T_{\rm int}$ is the integration time (Garnett & Forrest 1993). In this analysis, full integrations have a 1σ read noise of $\sigma_{\rm read} = 43\,{\rm me^{-}s^{-1}}$, corresponding to 2430 nW m^{-2} sr^{-1}.

The photon noise in this measurement is given by:

$$\sigma^2_{\rm photon} = \frac{6F(N^2+1)}{5T_{\rm int}(N^2-1)} \tag{3}$$

where F is the measured surface brightness at the detector. In these data, the typical surface brightness $F \approx 95\,{\rm me^{-}s^{-1}}$, yielding a typical $\sigma_{\rm photon} = 33\,{\rm me^{-}s^{-1}}$, which corresponds to 1840 nW m^{-2} sr^{-1}. The data presented here are read noise dominated by a factor of 1.3. Equations 2 and 3 predict that the measurement would have equal contributions from read and shot noise after ~ 140 s of integration time.

In this work we compute angular power spectra C_ℓ of images to investigate the spatial stability of the noise with time. Assuming uncorrelated white noise and ignoring sample variance, the power spectrum uncertainty δC_ℓ is given by:

$$\delta C_\ell = \sqrt{\frac{2}{f_{\rm sky}(2\ell+1)\frac{\Delta\ell}{\ell}}}(\sigma^2_{\rm pix}\Omega_{\rm pix}e^{\theta^2_{\rm beam}\ell^2}), \tag{4}$$

where $\Delta\ell$ is the band power bin width, $\sigma_{\rm pix}$ and $\Omega_{\rm pix}$ are the surface brightness rms noise and solid angle of each pixel, respectively, and $\theta_{\rm beam}$ is the point spread function width (Knox 1995).

3. Observations

We conducted our astronomical observations from the Jet Propulsion Laboratory's Table Mountain Test Facility (TMF) Astronomical Observatory[8]. As shown in Figure 4, LAMP was mounted on top of the 24″ telescope[9]. Doing so allows LAMP to use the existing pointing and tracking mechanism of the 24″ system. Because LAMP's optical axis was offset from the 24″ telescope's bore sight a small tracking error was introduced, an effect which we quantify in Section 4.2.

Sky observations were recorded for 03:30 to 13:00 during the night of February 15th, 2013 (UTC). Local astronomical darkness[10] began around 03:00 UTC, and a waxing crescent moon of $\approx$ 33 % illumination was present at low elevation early in evening, setting around 04:30 UTC.

[8]Longitude 117.7W, Latitude 34.4N, Altitude 2285 m asl.

[9]The TMF 24″ telescope is an Astro-Mechanics Ritchey-Chretien reflector on an off-axis German equatorial mount, see http://tmoa.jpl.nasa.gov for more information.

[10]See http://aa.usno.navy.mil/data/docs/RS_OneYear.php.

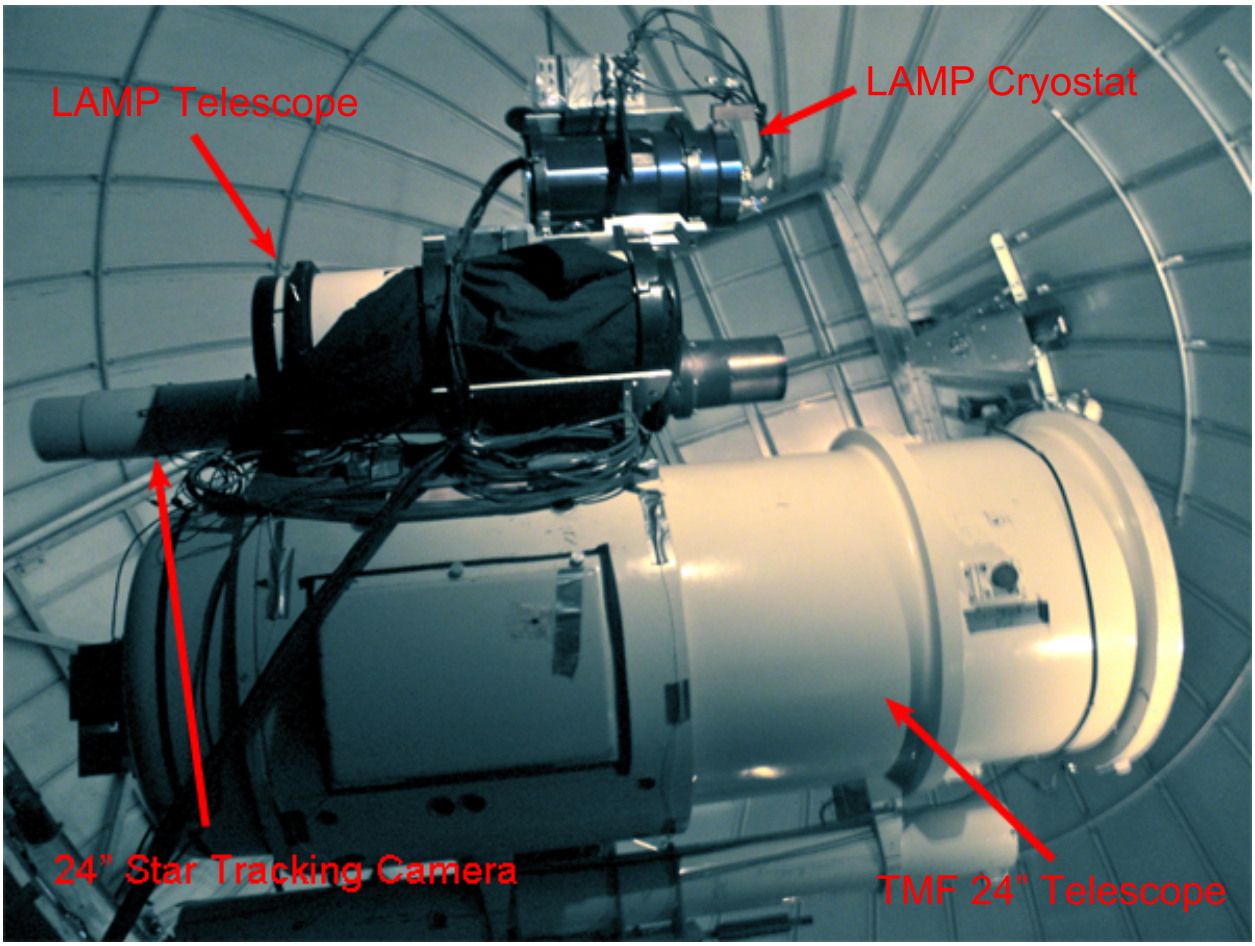

Fig. 4.— A photograph of LAMP mounted on the 24″ TMF telescope. The LAMP assembly is mounted to the larger telescope using an existing interface bracket. After installation, we verified the 24″ telescopes's pointing and tracking system, which to the level we were able to measure performed nominally under the additional load of the LAMP assembly.

After initial pointing calibrations, we observed the SWIRE-Lockman[11] Hole field centered at right ascension $10^{\rm h}45^{\rm m}$, declination $58°00'$ (referred to hereafter as the "Lockman" field). The data on which we report were recorded with the Lockman field at 45 degrees or more above the horizon (< 1.4 airmasses) over the night. The seeing was $\sim 2.5''$ throughout the night. Figure 5 shows the visibility of the Lockman field, the moon, and various other events throughout the observation period.

A total of 245 on-sky integrations were recored, with 232 of these having $T_{\rm int} > 105\,{\rm s}$. Of these, a large number were recorded during the early evening and early morning when the target field is low in the sky, and there are dynamic sources of emission beyond our control before midnight local time (for example, the fluorescent lighting and cars headlights associated with a local ski area).

The mean brightness of the fields reaches a constant plateau of $5330 \pm 30\,{\rm nW\ m^{-2}\ sr^{-1}}$ between 07:15 and 11:15 UTC over which no discernable time gradient is present. We call this set of 107 integrations "stable period" data. Of these, 10 integrations must be excluded as they do not meet the minimum $T_{\rm int}$ requirement, 5 must be excluded due to electrical pickup problems, and one must be excluded due to a tracking error. This leaves a set of 91 integrations which are sufficiently stable for analysis.

Dark frames are measured with the opening of LAMP telescope covered using a customized light-tight aperture cover. Data are acquired at regular intervals over the evening to monitor changes in the dark current. We measure an elevated dark current at the very beginning of the evening while the sky is darkening, likely due to light leaks and instabilities in the system. Over the course of the evening, the dark current drops to $\sim 0.25\,{\rm e^-s^{-1}}$ and is stable before and after the stable period. Approximately twenty dark integrations bracket the stable data period, and we use the mean and ensemble variance of these to be the dark current correction and error in that estimate.

Flat fields were measured during twilight, at the beginning and the end of the night. We take care to use only flat field frames in which the sky gives $S/N > 100$ per pixel but is not bright enough that non-linearities in the detector would become problematic, giving approximately twenty flat fields from which to compute the flat field correction.

4. Data Analysis

4.1. Low Level Data Analysis

The low level data reduction follows that presented in Zemcov et al. (2013a). For each integration, lines are fit to array reads 3 to 60, yielding a constant integration time of $58\,{\rm frames} \times 1.78\,{\rm s/frame} = 104\,{\rm s}$. The first two array reads are not used in the fit to reduce susceptibility to elec-

[11] http://irsa.ipac.caltech.edu/data/SPITZER/SWIRE/.

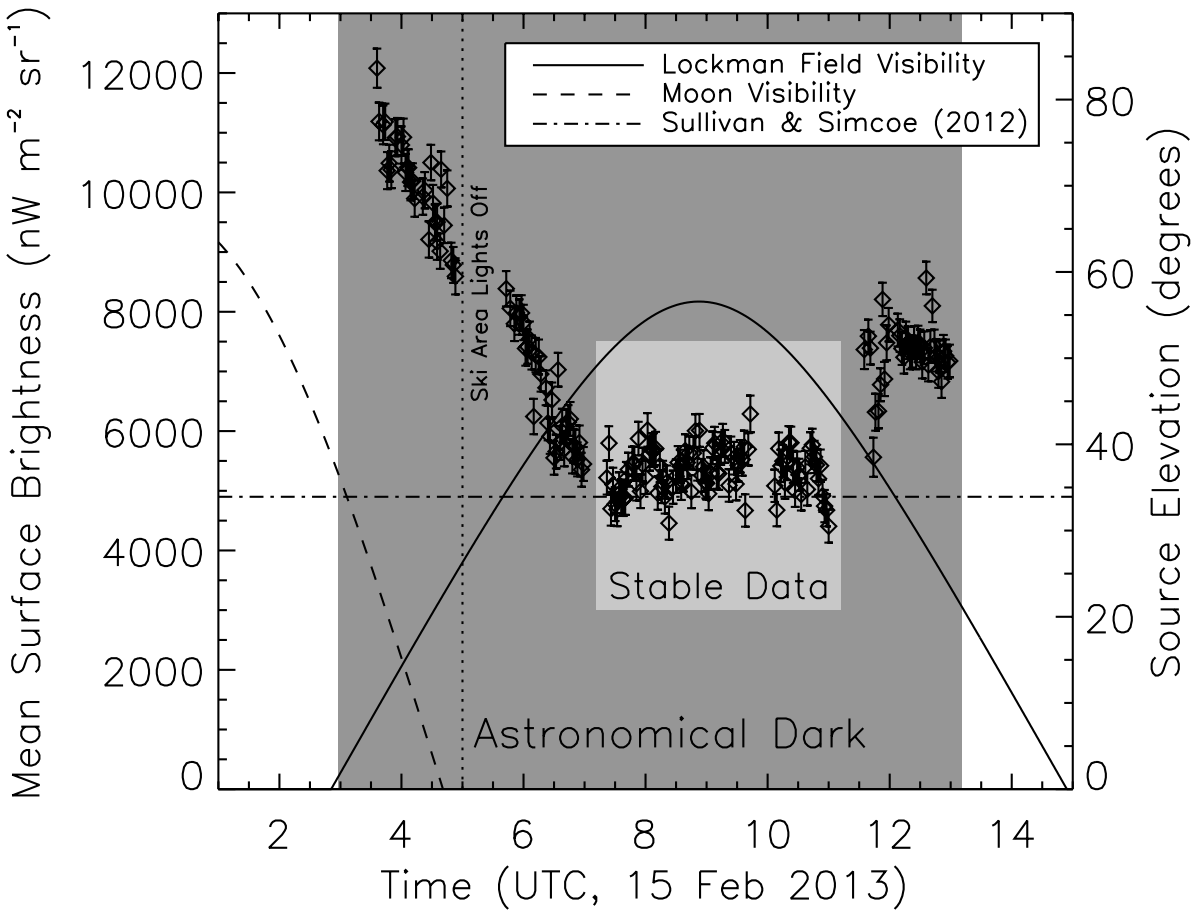

Fig. 5.— The derived near IR sky brightness as measured by LAMP on the night of 15 Feb, 2013 UTC from the Table Mountain Observatory. The astronomically dark period is indicated by the shaded area. The Moon (dashed line) set at approximately 04:30 UTC as the target field was rising (solid line). The TMF Observatory is located close to a skiing area whose Fluorescent lights are turned off at 05:00 UTC (22:00 local time). Airglow emission which is a function of the Lockman field's elevation is observed before and after a stable plateau in the sky surface brightness between 07:30 and 11:00 UTC (labeled "stable data"). These data are used in the stability study we present in this report. The small gap in the stable data near 09:30 are due to electronics errors and results from these integrations are not reported. The mean surface brightness of the sky is 5330 nW m^{-2} sr^{-1}, corresponding to $mag_{AB} = 19.7$, approximately 480 nW m^{-2} $sr^{-1}$of which can be attributed to Zodiacal light (Kelsall et al. 1998). This is close to the sky brightness at 1191.3 nm reported by Sullivan & Simcoe (2012) (dot-dashed line), measured by the FIRE instrument at an altitude of 2380 m from Las Campanas Observatory, Chile.

trical transients associated with array resets. The resulting photocurrents are calibrated to $e^- s^{-1}$ using known calibration factors which depend on the detector and electronics. Raw photocurrents of 0.25 $e^- s^{-1}$ are typical for these data.

After the photocurrent estimation, we correct for the dark current. We use the dark data discussed in Section 3 in each frame, where the photocurrent is estimated in the same way as for the sky integrations. The best dark current estimate is formed by computing the weighted mean of the individual dark frames that bracket the stable period integrations. We chose a weight function that weights according to the time difference between the sky integration being corrected and each dark frame t_{i-j} according to:

$$d_i = \sum_j t_{i-j}^{-1} d_j / \sum_j t_{i-j}^{-1} \tag{5}$$

where d_i is the dark current estimator for sky integration i, and d_j are the j individual measurements of the dark current. The effect of misestimating the dark current correction on our results is investigated in Section 5.3.

We generate a uniform-illumination responsivity response correction ("flat field") using the dedicated measurements presented in Section 3. To generate the flat field, we compute the sum of all eleven flat field measurements with photocurrents $100 < I_q < 350\, e^- s^{-1}$ to ensure detector linearity, and then divide by the sum of the median of each of the measurements. This weighting scheme is optimal in the limit that the integrations are dominated by photon noise, as is the case for $I_q > 50\, e^- s^{-1}$, and yields a measurement of the flat field which is normalized to have unity median. The effect of a systematic error in the estimation of the flat field correction on on our results is investigated in Section 5.3.

Next, the images must be registered to absolute astrometry to allow masking of known sources. This calculation is performed using the ASTROMETRY.NET[12] code which automates astrometric registration on arbitrary astronomical instruments (Lang et al. 2010). The accuracy of the astrometric solution is evaluated by computing the difference between the centroid of a subset of bright catalog sources and their positions given by the astrometric solution. This calculation is performed for all suitably bright sources in the image, producing sets of differences between the centroids and astrometry solution positions in both axes. For a given image we define the astrometric pointing error to be the standard deviation of each set of differences for each integration. To produce global values over the observing period, the above process was repeated for all stable period integrations. To determine the pointing error over the stable period, we fit a linear model to the time-ordered set of standard deviations in each axis. As a conservative estimate, the maximum values of the line fits over the stable period are taken to be the overall pointing error.

We calculate the overall pointing error as the mean ellipticity of an ellipse where the mean offset in right ascension and declination compose the semi-major and semi-minor axes. The total

[12]http://astrometry.net

uncertainty is 0.9″ in right ascension and 1.2″ in declination, yielding a total astrometric uncertainty of 1.0″.

The LAMP photometric calibration is calculated using stars from the 2MASS catalog (Skrutskie et al. 2006). Aperture photometry is performed on the twelve stars with $6 < J < 9.5$ in the LAMP images using a summing aperture of 10 pixels. The best fitting linear relation between the LAMP photometry and the known flux of the sources is then determined, yielding a calibration factor $\mathcal{C} = 5.52 \times 10^4\,\mathrm{nW\ m^{-2}\ sr^{-1}/\ e^{-}s^{-1}}$. We limit the uncertainty in the calibration to be 2.5 % using the nominal fitting error in the scaling between the LAMP photometry and 2MASS fluxes. The 2MASS photometric uncertainty is $\sim 1\,\%$, giving a total photometric calibration uncertainty of $\sim 3\,\%$. The calibration factor agrees with the theoretical calculation (listed in Table 2) within uncertainties.

As an example, we show an image to which the full data processing has been applied in Figure 6. In order to calculate power spectra from these images, the instrumental artefacts and images of stars must be masked, which in turn requires knowledge of the point spread function.

4.2. Point Spread Function and Source Masking

The LAMP point spread function (PSF) is estimated using a stack of sources similar to the method presented in Zemcov et al. (2013a). The core PSD is determined by stacking all 2MASS $J-$band catalog sources with $10 < J < 11$, and the extended PSF is determined by stacking all 2MASS sources with $5 < J < 10$. The full PSF is computed by splicing the two measurements together using a linear scaling in regions where the PSF is between 1 % and 10 % of its peak in the core stack. An example of the PSF stack result in a single integration is shown in Figure 7.

For each integration, we estimate the width of the PSF by fitting a two-dimensional Gaussian to the PSF stack. The mean one-dimensional PSF width is estimated from the average of the semi-major and semi-minor widths of the best fitting result. The mean FWHM value over the entire data set is 8.5″, but is variable with time from 8.0″ at the beginning of the stable data region to as poor as 9.5″ at the end. It is not clear what causes this degradation, but other than the $\sim 20\,\%$ broadening in both axes no trend in ellipticity is detected.

The total PSF width is the quadrature sum of several contributions, including the intrinsic PSF, the focus of the telescope, pointing errors, and atmospheric seeing. The contribution from each of these contributions is summarized in Table 3.

The instrument's intrinsic PSF FWHM is estimated as equal to the full width of the 68 percent encircled energy contour in a ray trace simulation. Though the encircled energy diagram changes slightly over the array, this contour is always less than 25 μm, corresponding to 6″.1 at the 18 μm pixel pitch of the array.

Over the course of an integration the instrument pointing may not perfectly track the sky,

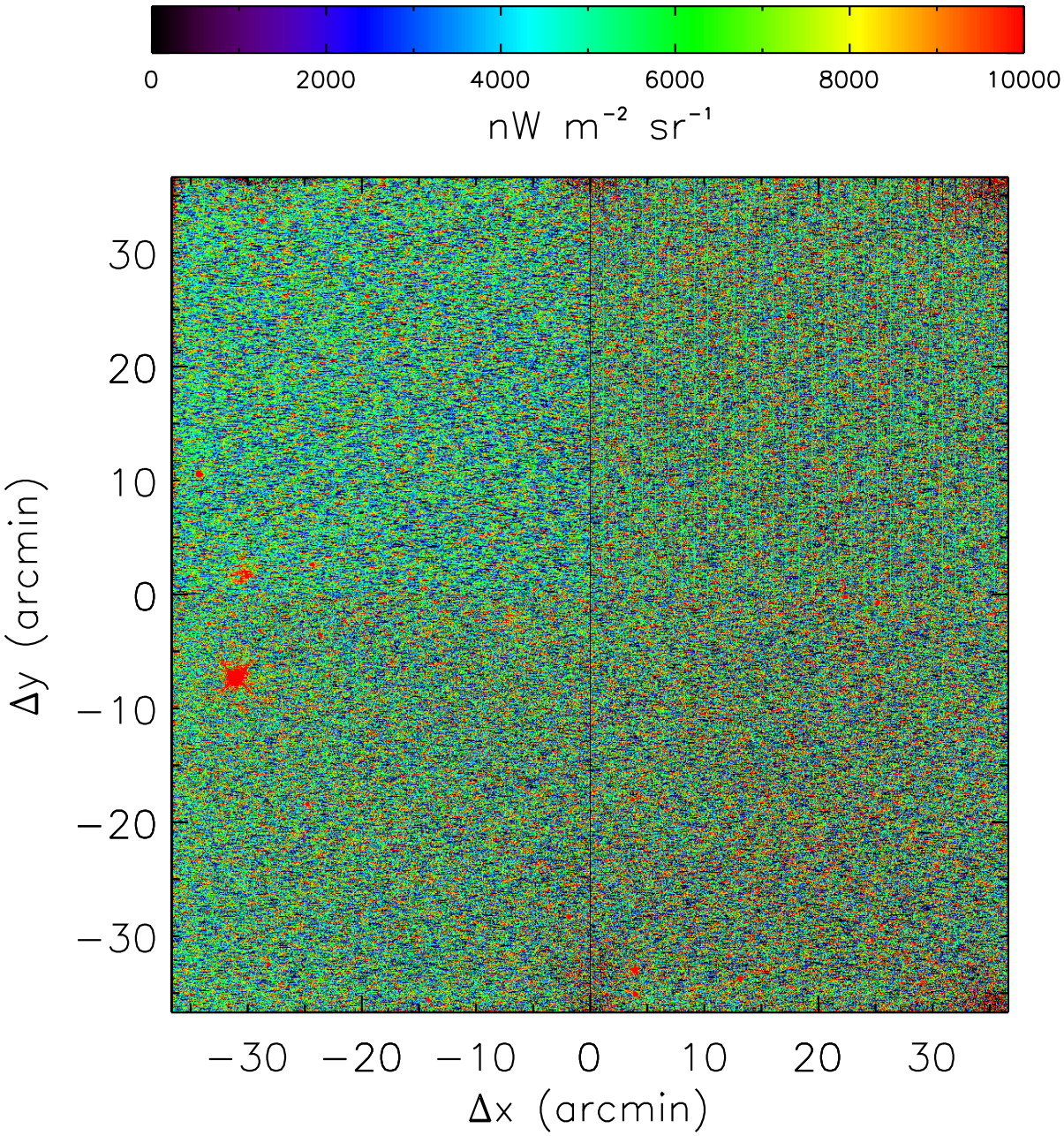

Fig. 6.— A raw $T_{\rm int} = 104\,{\rm s}$ integration on the Lockman field at 1191.3 nm as seen by LAMP. The image has had dark current subtraction and flat field responsivity correction applied. The pixel size is $4.3''$ on a side, giving a field of view of 1.5 square degrees centered at $10^{\rm h}47^{\rm m}17^{\rm s}$, $57^\circ53'30''$. Several features are apparent in this image, including an image of the $J = 3.13$ star HD 93132 near $(-32, -7)$ with diffraction spikes from the secondary mirror support, a reflection of its image near $(-32, 2)$, pixels with large multiplexer glow and fabrication defects around the edges of the array, and unresponsive columns in the upper right hand quadrant. These features, as well as bright stars and galaxies in the 2MASS catalog, are masked later in the analysis.

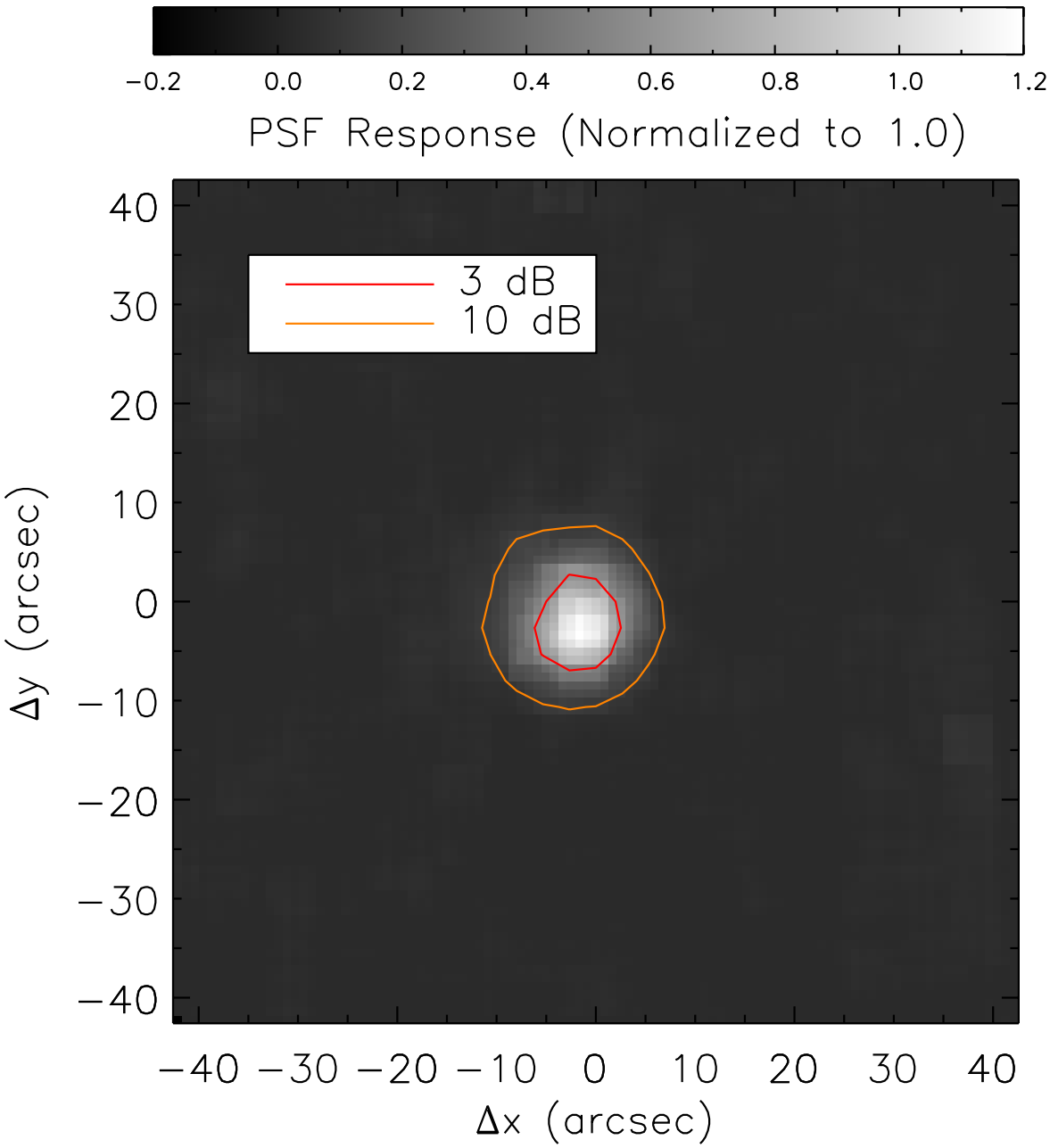

Fig. 7.— The LAMP PSF measured in a single integration on a 3× sub-sampled pixel grid. To measure the PSF, we combine stacks on all stars with $5 < J < 10$ for the extended PSF, and $10 < J < 11$ for the core PSF, which yields a determination of the overall PSF sufficient to allow accurate source masking. The contours show the 3 dB (i.e. the FWHM) and 10 dB contours of the PSF smoothed to LAMP's native pixelization.

Table 3: Point Spread Function Width Budget

Component	Contribution (FWHM)
Intrinsic PSF Width	$6''.1$
Pointing Errors	$1''.5$
Atmospheric Seeing	$2''.5$
Total Calculated PSF Width	$6''.8$
Total Measured PSF Width	$8''.5$
Inferred Defocus	$5''.1$

either coherently with time ("smear") or as a random noise ("jitter"), and degradation of the PSF width could result. To constrain pointing smear, we compute the difference between the astrometry solutions in two time-halves of the same full integration, which in the absence of smearing should be zero. The astrometry solution is independently determined for each half-integration, and the difference between them is computed. This procedure yields a mean difference of $1''.0$ over the stable data period, with no evidence for ellipticity. To constrain pointing jitter, we calculate the difference between the known catalog positions of all $5 < J < 10$ sources and their positions from the per integration astrometry solution. For each integration, we then compute the mean difference over all sources, yielding a monitor of the overall accuracy of the astrometric solution over time. The mean difference between the known and solved positions of catalog sources over the stable data period is $\delta\theta = 1''.1$, and we detect no significant difference between right ascension and declination or time variation. Assuming the pointing jitter and smearing are uncorrelated so they may be added in quadrature, we estimate the total pointing error to contribute $1''.5$ to the PSF width.

The atmospheric seeing was recorded as $2''.5$ during the observation period.

The measured PSF width differs from the sum of the various contributions by $\sqrt{8''.5^2 - 6''.8^2} = 5''.1$. This is likely due to poor focus of the instrument, which was mechanically set during laboratory testing and could not be verified after mounting at TMF. These could be discrepant due to alignment errors during instrument mounting.

Having determined the PSF, the images can be masked. The masking algorithm follows that presented in Zemcov et al. (2013a), with $\alpha_m = -8''.5\,\mathrm{mag}^{-1}$ and $\beta_m = 141''.0$, resulting in a slightly broader mask than used for the CIBER data. As in the Zemcov et al. (2013a) analysis, these parameters are determined by computing the power spectra of simulations of the 2MASS sources in the image and estimating the threshold at which the power from residual sources is significantly less than the noise in the image. In the LAMP analysis, we mask to $J = 16\,\mathrm{mag}$, as the per integration surface brightness sensitivity is significantly larger than this source flux. Between astronomical sources and masks of static structure on the detector typically 16 % of pixels are masked.

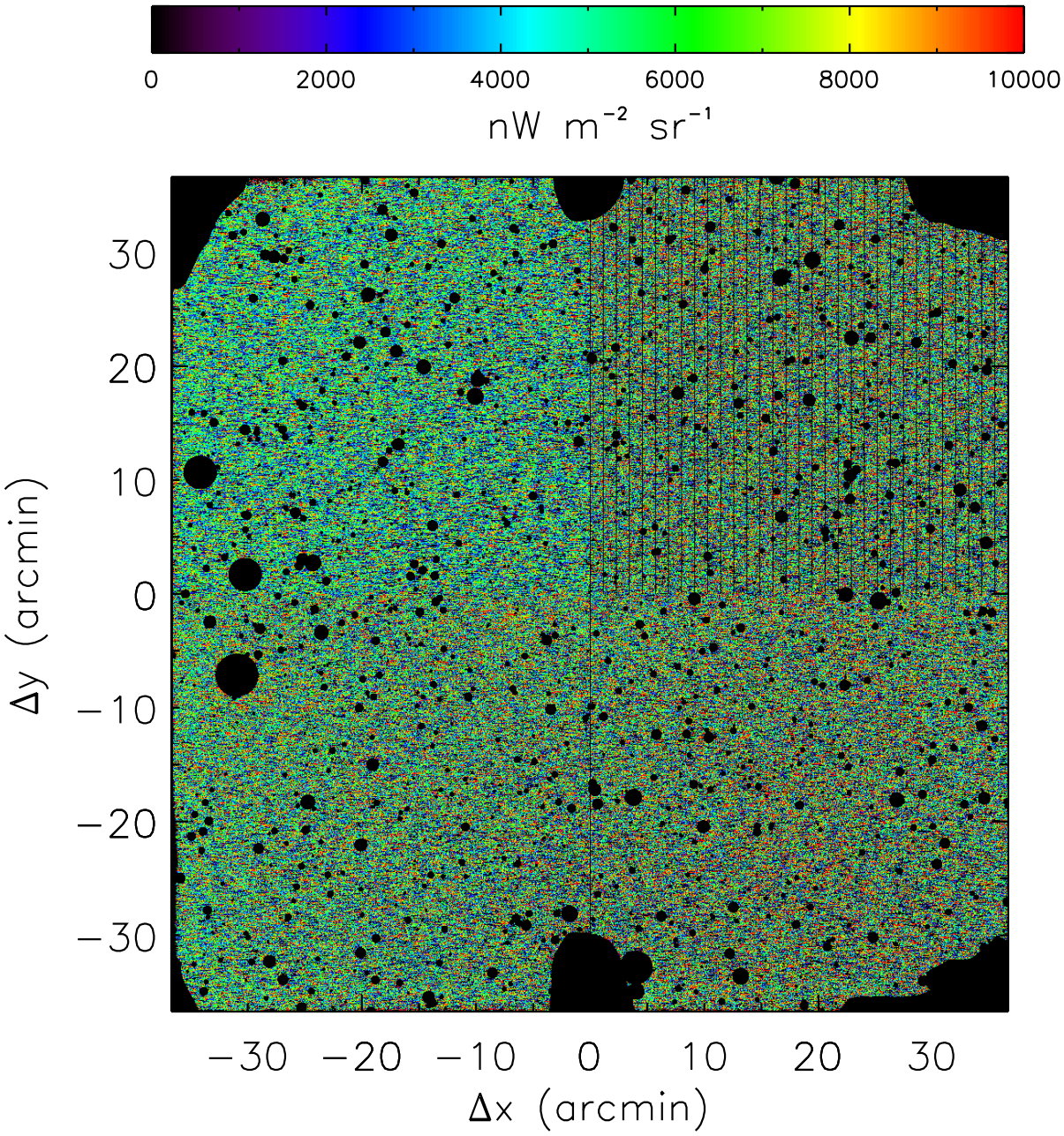

Fig. 8.— The same array integration as shown in Figure 6, but with masking of array defects and $J > 17.5$ astronomical sources applied. Approximately 16 % of pixels are lost to the mask. The resulting image structure is consistent with a combination of read noise and shot noise from the diffuse airglow emission.

4.3. Power Spectrum Estimation

The spatial auto-power spectra are computed using a version of the MASTER formalism (Hivon et al. 2002) in which the true sky $\widetilde{C_\ell}$ is related to the measured sky power $\langle C_\ell \rangle$ by:

$$\widetilde{C_\ell} = \sum_{\ell'} M^{-1}_{\ell\ell'} \frac{(\langle C_{\ell'} \rangle - N_{\ell'})}{B^2_{\ell'}}, \tag{6}$$

where $M_{\ell\ell'}$ is the mode-mode coupling matrix, N_ℓ is the noise bias, and B_ℓ is the beam transfer function. The details of the implementation of this algorithm are identical to the analysis of CIBER data which uses the same detector, and can be found in the Supplementary Materials to Zemcov et al. (2013a).

5. Results

These data allow us to determine both the brightness of the atmosphere and the temporal stability of the atmospheric emission from ~ 10 to ~ 100 s time scales.

5.1. Sky Brightness and Image Noise

The per-integration mean sky brightness shown in Figure 5 is computed by calculating the mean image brightness in the unmasked regions of the calibrated images. Since stars with $J > 16$ are masked, the brightness is dominated by atmospheric emission with a brightness of ~ 5000 nW m^{-2} sr^{-1} and a small contribution from Zodiacal light (ZL) with a brightness of ~ 300 nW m^{-2} sr^{-1}(Kelsall et al. 1998). The mean sky brightness over the entire stable data period is 9.57×10^{-2} e$^-$s^{-1}, which corresponds to 5330 nW m^{-2} sr^{-1}, as shown in Figure 5. The root mean squared variation over this period is ± 30 nW m^{-2} sr^{-1}. There is no evidence for a temporal drift in the brightness of the images during the stable period.

Because of the OH emission, it is impossible to draw meaningful comparisons between measurements of the band-averaged $J-$band sky brightness (see e.g. Leinert et al. 1998) and our measurement of the inter-line sky brightness. However, the LAMP measurement can be compared directly with the result of Sullivan & Simcoe (2012) who determined the inter-line continuum between 0.83 and 2.5 μm at $R = 6000$ using Magellan/FIRE from Las Campanas in Chile. At the LAMP operating wavelength of 1191.3 nm, they find $\lambda I_\lambda = 19.8 \pm 0.15$ mag$_{\rm AB}$ arcsec^{-2}. They further find mean sky brightnesses in $Y-$ and $J-$band of 20.05 ± 0.04 and 19.55 ± 0.03 mag$_{\rm AB}$ arcsec^{-2} respectively, which at 1191.3 nm interpolates to 5287 ± 128 nW m^{-2} sr^{-1}, in good agreement with our determination. This is evidence that, once time-dependent emission has quieted, the inter-line continuum at this wavelength is not dominated by terrestrial light pollution (Leinert et al. 1998). Sullivan & Simcoe (2012) show that their measurements are consistent with previous measurements

at 1.6 μm where the inter-line background is up to 0.7 $\mathrm{mag_{AB}}$ $\mathrm{arcsec^{-2}}$ brighter (Maihara et al. 1993, Cuby et al. 2000, Ellis et al. 2012).

We can also use the Gemini Observatory sky model[13] to compute the atmospheric emission spectrum. The model is computed with the sky transmission files generated by ATRAN (Lord 1992) scaled to a 273 K blackbody. We assume 5 mm of precipitable water vapor during our measurements, which is consistent with the typical value above Table Mountain during clear weather (Leblanc et al. 2011), and find a prediction of 19.5 $\mathrm{mag_{AB}}$ $\mathrm{arcsec^{-2}}$ from the model. Subtracting the estimate for ZL emission, this is $\sim 25\,\%$ greater than our measurement, which also agrees with the conclusion of Sullivan & Simcoe (2012) that the Gemini model over-predicts the inter-line sky brightness at $J-$band by a similar factor.

In addition to the mean brightness, it is useful to calculate the image noise properties to show they track the simple theoretical predictions discussed in Section 2.2. This allows us to diagnose whether there is some gross source of excess noise in the system. The theoretical noise properties are calculated from the quadrature sum of the read and photon contributions given by Equations 2 and 3. Table 4 summarizes the theoretical noise characteristics of these LAMP measurements given the parameters listed in Table 2. From the ratio $\sigma_{\mathrm{read}}/\sigma_{\mathrm{photon}}$ we conclude that these 104 s integrations are read noise dominated by a factor of 1.3. At the measured sky brightness, the integrations should become photon noise dominated after 136s of integration.

Table 4: LAMP Characteristic Noise Properties.

σ_{read}	$4.4 \times 10^{-2}\,\mathrm{e^{-}s^{-1}}$
Sky $\langle \lambda I_\lambda \rangle$	$0.96 \times 10^{-2}\,\mathrm{e^{-}s^{-1}}$
σ_{photon}	$3.3 \times 10^{-2}\,\mathrm{e^{-}s^{-1}}$
$\sigma_{\mathrm{read}}/\sigma_{\mathrm{photon}}$	1.3
σ_{total}	$5.5 \times 10^{-2}\,\mathrm{e^{-}s^{-1}}$
Theoretical σ_{total}	$3.05 \times 10^{3}\,\mathrm{nW\ m^{-2}\ sr^{-1}}$
Measured σ_{total}	$3.07 \pm 0.08 \times 10^{3}\,\mathrm{nW\ m^{-2}\ sr^{-1}}$

To compare the noise properties of the data images to the predictions, we compute the standard deviation of unmasked pixels in time-wise full-integration pair differences. We remove variance from faint sources of astronomical emission by aligning the two input integrations with each other using the astrometry solution, leaving a set of 45 differences in the data set. The pixel distribution in the differenced images matches a Gaussian distribution whose width is $\sqrt{2}$ larger than σ_{read} listed in Table 4. The variance in the width of the noise distribution is given by $S^2_{\mathrm{error}} = \sigma^2_{\mathrm{total}}\sqrt{2/(n-1)}$ where n is the number of unmasked pixels and S^2_{error} is the variance in the standard deviation. These are shown in Figure 9 for each pair-wise integration difference in the stable period data set.

[13] http://www.gemini.edu/sciops/telescopes-and-sites/observing-condition-constraints/ir-background-spectra#Near-IR-short

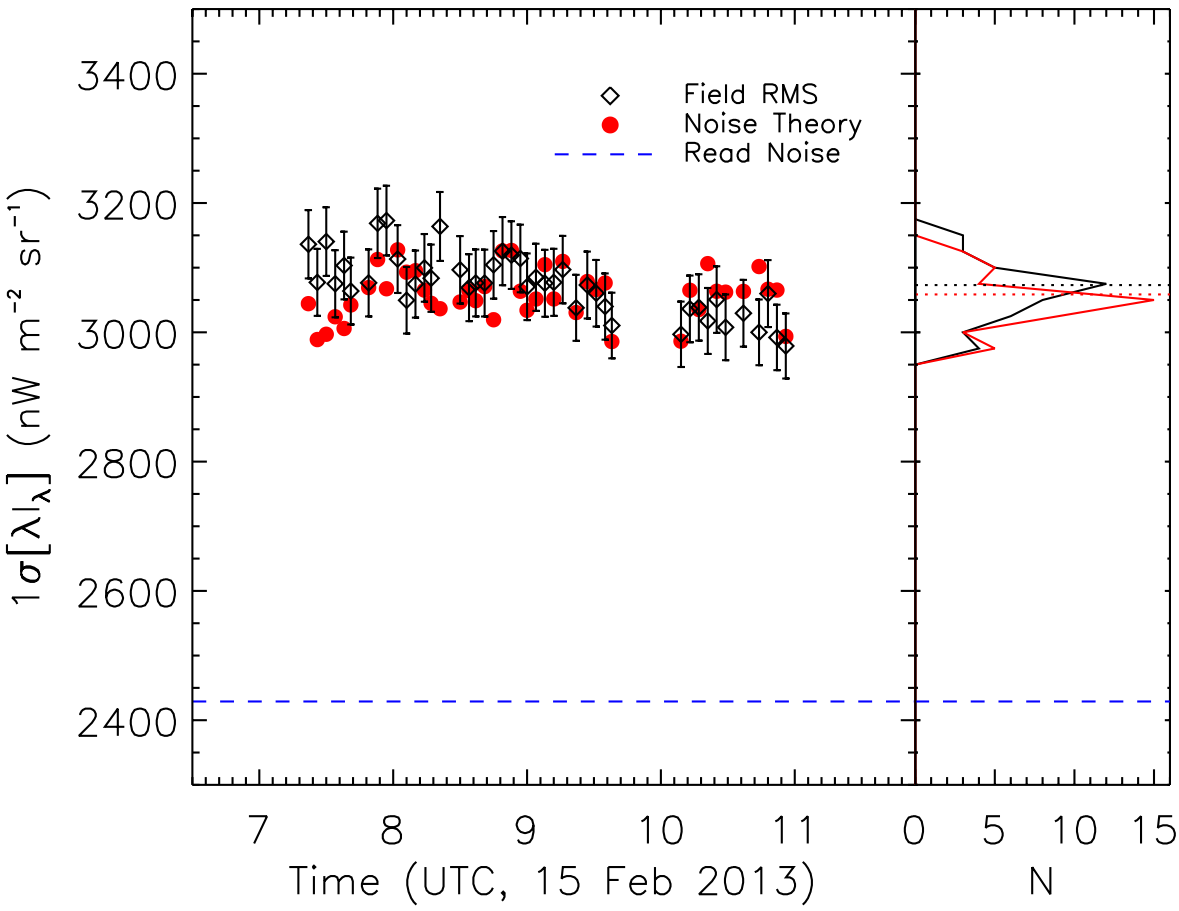

Fig. 9.— Image-space noise over time. The image space noise is estimated by computing the standard deviation of unmasked pixels in pair-wise differences of the stable data integrations (diamonds). The plotted uncertainties are the errors on the standard deviation. Also shown are the predictions from noise theory for the noise in each measurement (circles) calculated with the mean surface brightness of the field pairs to calculate the shot noise term. The read noise is modelled as static over time (dashed line). There is a weak downward trend in the noise properties of the images over time, but it is not clear whether this is due to some property of the instrument, to slight changes in the mean surface brightness of the sky over time, or random statistics. In the right hand panel we show histograms of the points (solid lines) with the mean of both distributions indicated (dotted lines). The χ^2 of (data - theory) is 48.8 for 44 degrees of freedom, giving a probability to exceed χ^2 of 0.29. We conclude that there is no evidence for an extra noise component in the image data.

The mean uncertainty over the stable period data is found by computing the uncertainty-weighted mean of difference images, giving $3070 \pm 80\,\mathrm{nW\ m^{-2}\ sr^{-1}}$, where the total uncertainty is estimated from the noise weights. To check for consistency between the theoretical estimate and measure noise performance, we compute the χ^2 of the data and theory points shown in Figure 9 and find a probability to exceed χ^2 of 0.29, indicating consistency between the estimates even assuming simple the uncorrelated read noise at the level shown in Table 4.

5.1.1. Sub-integration Image Noise Properties

An important component of this study is an investigation of the noise behavior over intervals shorter than a full 104 s integration. To do this, we calculate estimates for the photocurrent for fractional parts of the full integration length, subtract adjacent fractional integrations, and calculate the noise in the same manner as for the full integrations. The variation of the mean values are calculated in the same way as for the full integration differences. Because the full integration time is ~ 100 s, we have two possible populations of such differences: (i) differences of sub-integrations in the same integration, limited to $T_{\rm int} < 51$ s, and (ii) differences of sub-integrations in neighboring integration sets, which allow us to add points $52 \leq T_{\rm int} \leq 104$ s. Measurements of the latter type are actually separated by > 104 s rather than being truly temporally contiguous, but they allow us to map out the reduction in noise with integration time which should follow the quadrature sum of Equations 2 and 3.

Correlated noise could modify the relationship between difference pair noise RMS and $T_{\rm int}$ at short integrations. As discussed in Bock et al. (2013) and Zemcov et al. (2013a), the HAWAII-1 detectors used in LAMP have correlated noise on the output with correlation lengths of several seconds, so differencing on short time scales may actually reduce the measured noise figure. To check for this, we compute the cross-correlation of the images from adjacent integrations for sub-integrations of the first type (for $T_{\rm int} < 51$ s). The resulting correlation coefficients are shown in Figure 10.

The short $T_{\rm int}$ difference images are correlated, as we might expect for amplifier noise. We do not measure a correlation in the sub-integration differences taken with neighboring data sets. To correct the measured noise RMS for this correlation, we compute:

$$\sigma'_{i-j} = \frac{\sigma_{i-j}}{1-r} \tag{7}$$

where σ_{i-j} is the measured RMS in the difference between sub-integrations i and j, r is the measured correlation between them, and σ'_{i-j} is the corrected pixel RMS. There is no evidence for correlations between differences involving sub-integrations drawn from separate major integration intervals.

The pixel RMS in both types of sub-integration measurements are shown in Figure 11 as a function of the effective integration time. For the first-type sub-integration difference RMS, we

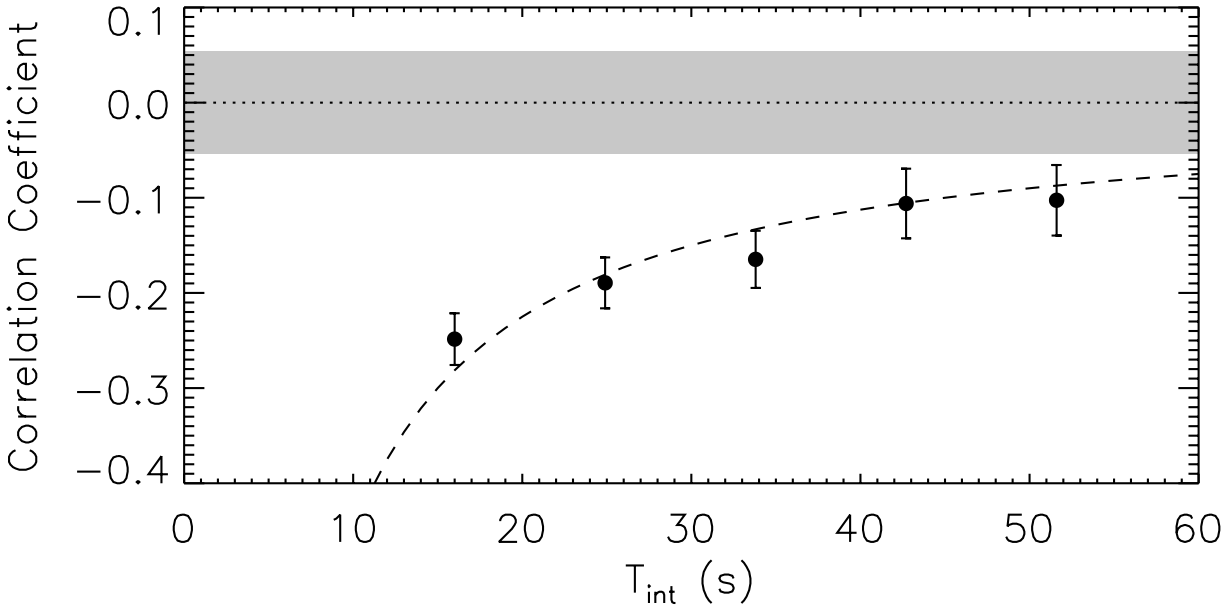

Fig. 10.— Correlation coefficient of sub-integration fits drawn from the same integration. Because each read in a pixel of a charge integrating detector is correlated with the previous read, sub-integrations are mildly correlated with one another. We empirically determine the correlation coefficient r between the sub-integrations sharing a full integration, and plot the mean and standard deviation versus $T_{\rm int}$. The scaling is well explained by $1/T_{\rm int}$ (dashed line). The correlation coefficient of neighboring full integrations are not correlated, and have a standard deviation about zero shown as the grey band.

correct for the effects of the correlation, and plot σ'_{i-j}. The model effectively predicts the behavior of the noise RMS within the uncertainties.

5.2. Spatial Fluctuations

We measure the time variation in spatial fluctuations in the sky emission using auto-power spectrum measurements. To constrain a hypothetical component associated with variations in the continuum level between the Meinel bands, it is necessary to account for the other sources of power in the power spectrum, namely: (i) astronomical emission $\widetilde{C_\ell}$; (ii) noise bais from the detector $N_\ell^{\rm read}$; and (iii) noise bias from photon noise $N_\ell^{\rm photon}$. To account for these, we can begin by writing equation 6 in a slightly different form in which we solve for the measured sky and ignore the effects of image masking:

$$\langle C_\ell \rangle = B_\ell^2 \widetilde{C_\ell} + N_\ell, \tag{8}$$

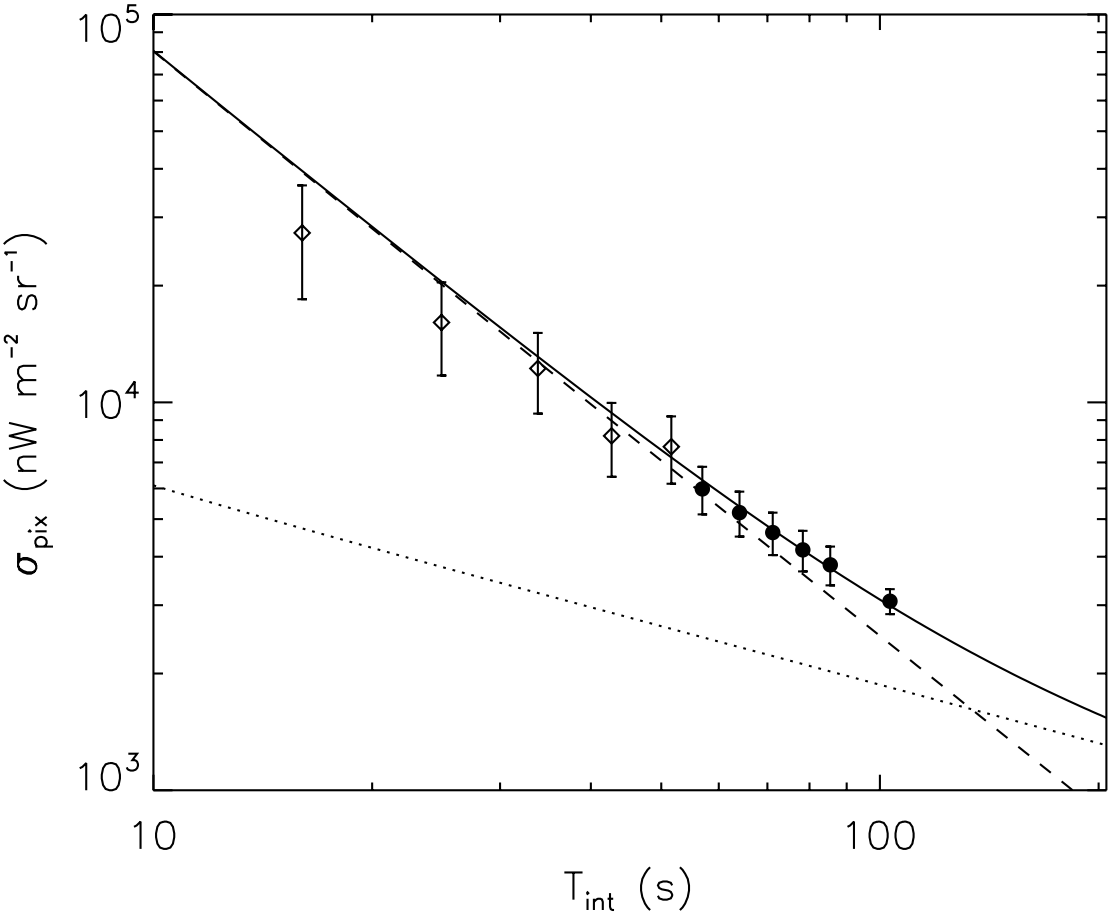

Fig. 11.— The pixel standard deviation in differences of neighboring integrations (solid circles) or sub-integrations sharing a full integration (open circles) versus integration time. The sub-integration points have been corrected for the effect of noise correlations using the empirical scaling shown in Figure 10. In the absence of extra noise components, the points should follow the sum (solid line) of shot noise (dotted line) and read noise (dashed line). Known noise components explain the behavior of the image space pixel noise as a function of integration time.

where $N_\ell = N_\ell^{\rm read} + N_\ell^{\rm photon} + N_\ell^{\rm sky}$, where $N_\ell^{\rm sky}$ is the hypothetical component of the noise due to time variations in the spatial emission of the atmosphere.

Ideally, to isolate $N_\ell^{\rm sky}$, we would difference away the other terms in the sum in Equation 8. The $\widetilde{C_\ell}$ term is common to neighboring integrations, and so can be cancelled by differencing neighboring integrations which have been aligned to one another. However, because the noise is different in each realization of the measurement it is not possible to cancel the N_ℓ terms through differencing of data alone. Rather, to isolate this component, we observe that from Equations 2 and 3 the time-dependence of the components $N_\ell^{\rm read}$ and $N_\ell^{\rm photon}$ can be inferred. That is, by differencing integrations aligned to one another $\widetilde{C_{\ell,1}} = \widetilde{C_{\ell,2}}$, so we have:

$$\begin{aligned}\langle C_\ell^{\rm diff}\rangle &= N_{\ell,1}^{\rm read} + N_{\ell,1}^{\rm photon} + N_{\ell,1}^{\rm sky} + N_{\ell,2}^{\rm read} + N_{\ell,2}^{\rm photon} + N_{\ell,2}^{\rm sky} \\ &= (N_{\ell,1}^{\rm read} + N_{\ell,2}^{\rm read})(T/T_0)^{-3} + (N_{\ell,1}^{\rm photon} + N_{\ell,2}^{\rm photon})(T/T_0)^{-1} + (N_{\ell,1}^{\rm sky} + N_{\ell,2}^{\rm sky}),\end{aligned} \tag{9}$$

this is equivalent to:

$$\langle C_\ell^{\rm diff}(t)\rangle = a_{\rm read}T^{-3} + a_{\rm photon}T^{-1} + a_{\rm off}, \tag{10}$$

where $\langle C_\ell^{\rm diff}\rangle$ is the difference power spectrum and the a_i are constants of proportionality related to N_ℓ. The scheme we use here is to measure $\langle C_\ell^{\rm diff}\rangle$ as a function of time and to constrain a component which does not behave as either of the known noise components. We note that by using this model we are constraining a time-invariant term in the noise $a_{\rm off}$ which we correspond to the $N^{\rm sky}$ term, and that we would not be at all sensitive to an excess component which behaves as either T^{-3} or T^{-1}. Since this is a preliminary measurement, and we expect any deviation from the expected behavior of the noise to change slowly with $T_{\rm int}$, constraining the simplest possible model (*i.e.* an offset in the model) is a conservative approach.

Figure 12 shows the full set of $\langle C_\ell^{\rm diff}\rangle$ for the set of 45 full-integration time difference field data scaled to the non-differenced amplitude. The predicted effective sensitivity for the combined 3.5 hrs of integration lies above the ideal sensitivity calculated assuming uncorrelated white noise with $\sigma = 3.07\times10^3$ nW m^{-2} sr^{-1}. Because these detectors have complex noise properties (Zemcov et al. 2013a), the simple comparison is not diagnostic as the excess noise component may be due to read noise correlations, or a component due to sky variability.

To succinctly compress the power information in the power spectra, for each $T_{\rm int}$ we compute the mean of all bandpowers in two broad bins, one between $10^3 < \ell < 10^4$ and the other $10^4 < \ell < 10^5$, as shown in Figure 13. As these two regions are made flat with different ℓ scalings, we chose a multiplicative prefactor of $1/2\pi$ in the lower-ℓ region and $\ell^{0.75}/2\pi$ in the higher-ℓ region. This allows us to compute a mean over a region with approximately the same value.

The time-dependence of the bandpower averages is shown in Figure 14, which show the mean of the two ℓ regions versus $T_{\rm int}$ for all differencing time scales we probe in this measurement. The $T_{\rm int} < 55$ s difference sets, which are computed from the same integrations, are corrected by a factor of r^2 to account for their correlation. To constrain the value of $a_{\rm sky}$ in Equation 10, we fit a function of that form to the scaled mean as a function of $T_{\rm int}$. The fit results in an offset consistent with

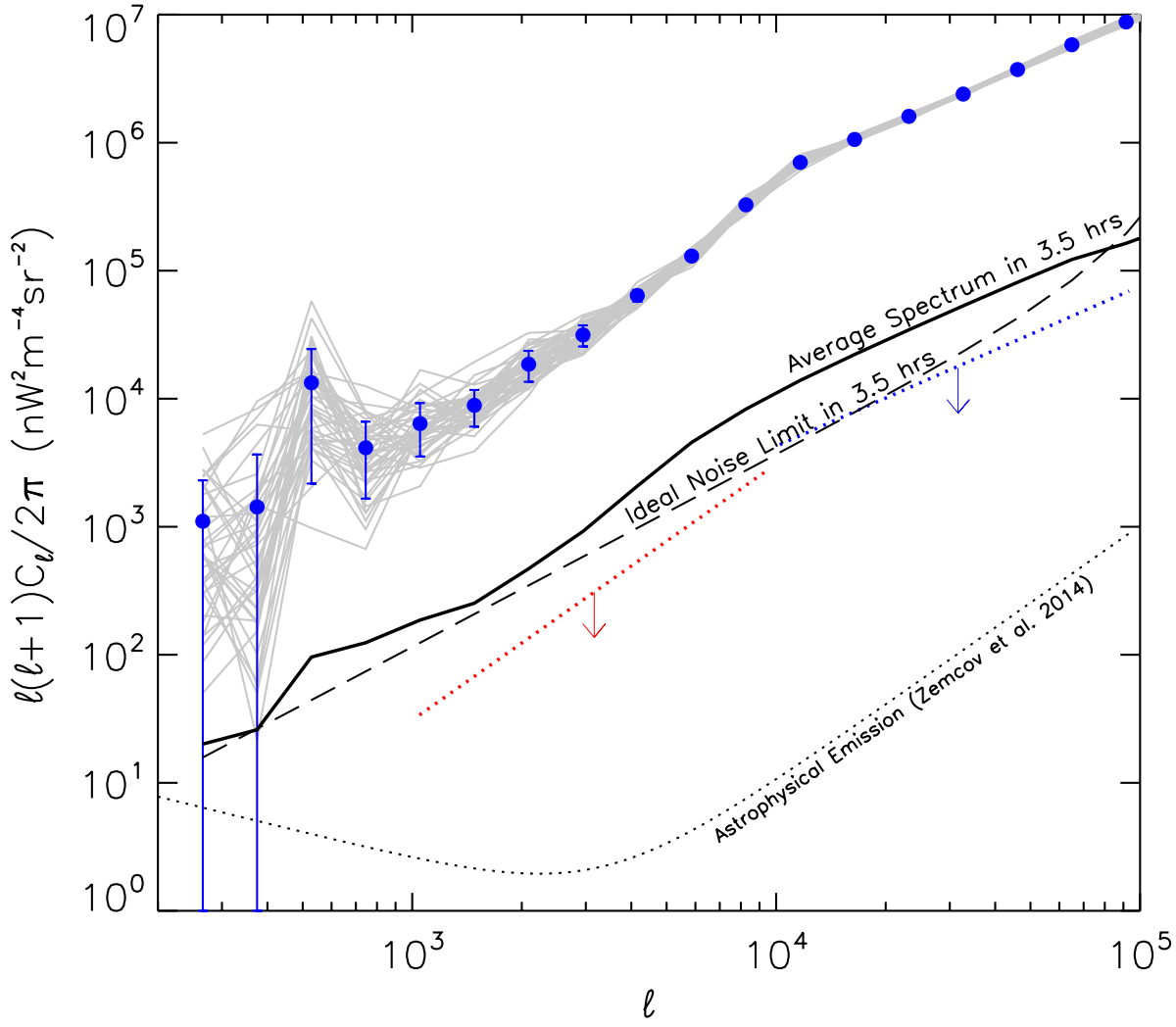

Fig. 12.— LAMP power spectra for full integration time field differences. The grey lines show the individual power spectra for each of the 45 differences. The blue points show the mean power spectrum, with uncertainties plotted encompassing the per bandpower standard deviation over the ensemble. The solid black line shows the total sensitivity reached by averaging all of the individual integrations together, and the dashed black line shows the theoretical statistical sensitivity in the full data set assuming uncorrelated white noise. Though there is evidence for some excess noise above the ideal noise limit, it is difficult to assign to correlated read noise or an excess noise component from this plot alone. The red and blue dotted lines show 2σ upper limits to a component of the noise that does not follow the time-dependence of either read or photon noise. We find no evidence for an excess component in the noise to the limit of the measurement. The dotted line shows the fiducial astrophysical power spectrum for $J > 17.5$ source masking measured by Zemcov et al. (2013a). The noise is larger than the astronomical power from IHL, but 250 hours of integration time would decrease to interesting levels a factor of ~ 70 lower than the currently achieved noise.

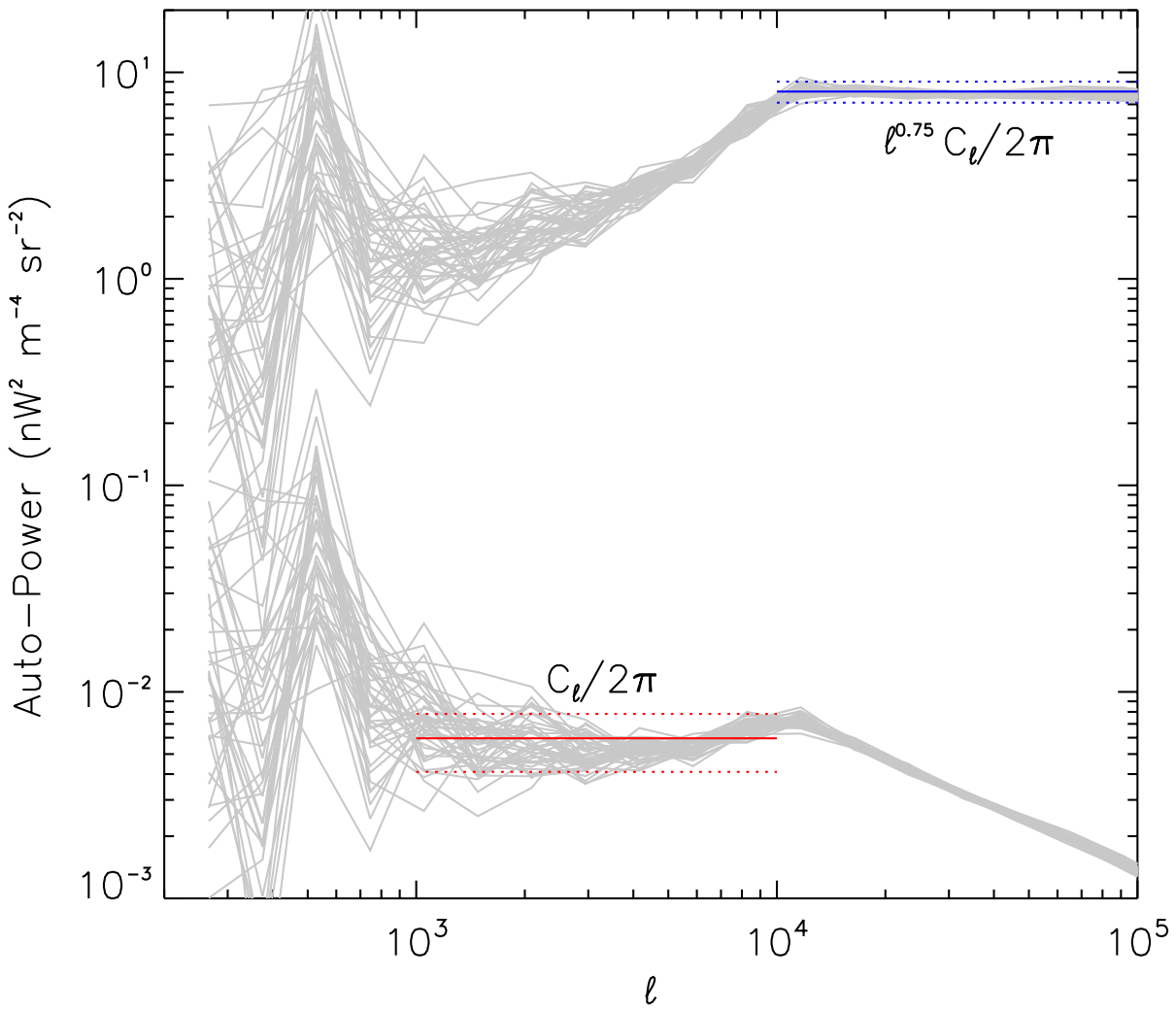

Fig. 13.— The LAMP power spectra show in Figure 12 using different scalings. The pre-factors, $1/2\pi$ in the $10^3 < \ell < 10^4$ region and $\ell^{0.75}/2\pi$ in the $10^4 < \ell < 10^5$ region, are chosen to make the power approximately constant in the regions of interest. We ignore the $\ell < 10^3$ region due to large variance. The mean and standard deviation of the set of 45 measurements in the two regions are indicated by the solid and dashed lines. These statistics are calculated for the full set of $T_{\rm int}$ measurements to develop the behavior of the noise with integration time.

zero within uncertainties, which is good evidence there is not a component of the noise which does not scale with integration time. To place limits on the amplitude of this component in the power spectra, we compute the 2σ upper limit from the best-fitting value of $a_{\rm off}$ and compute its ratio to the $T_{\rm int} = 104\,{\rm s}$ point in Figure 14. We then scale the amplitude of the power spectra shown in Figure 12 at the mean bandpower by this ratio to generate an upper limit on the atmospheric variation as a function of ℓ, as shown in Figure 12. We do not detect an excess noise component which does not scale with time in these data.

5.3. Systematic Uncertainties

The major systematic uncertainties which affect this work are the dark current and flat field corrections. To place limits on these, we compute the power spectra in the following cases: (i) when no flat field is applied; (ii) when the dark current correction is varied by its uncertainty in the positive direction; and (iii) when the dark current correction is varied by its uncertainly in the negative direction.

We motivate the flat field systematic check by noting that the photocurrent at the detector is very small, so the gain errors have a very small effect compared to the variance of the measurement. In measurements of the mean or variance of images, the flat field correction will have very little effect since it is referenced to the mean of the measurements. The flat field will have more of an effect in power spectral measurements, as it has spatial coherence over large scales in the array (Bock et al. 2013). As a result, we expect that the flat field will have little effect except at low ℓ modes.

Because of the low photocurrent in these measurements, the dark current correction is the single most important source of systematic uncertainty. The dark current estimate, which is formed per pixel from the ensemble variance of the dark current measurements, has small uncertainties, but both the correction and its uncertainties do exhibit large scale structure, so we are most concerned about the presence of systematic uncertainties in the spatial power spectra. We place limits on the effect of the dark current correction by computing power spectra in which the dark current correction is varied by its 1σ uncertainty in both the positive and negative directions. This simulates the effect of over- and under-estimating the dark current correction, respectively, and is a conservative upper limit to the size of the possible coherent effect we would expect.

Figure 15 shows the systematic uncertainties arising in the power spectra from these tests. The systematic uncertainties are typically manageable for $\ell < 10^3$ where they are $< 20\,\%$ at all bandpowers, and $< 5\,\%$ for $\ell < 3000$. As expected, the flat field correction is the largest source of systematic uncertainty, showing systematic deviation above the fiducial power spectrum for $\ell < 3000$, and below it for $\ell > 3000$. We propagate these power spectra systematic errors to upper limits on the atmospheric noise component shown in Figure 12 and summarize the results in Table 5. We quote $\ell(\ell+1)\langle\delta C_{\ell,{\rm sky}}\rangle/2\pi$, which here we define to be the 2σ upper limit on auto-power over

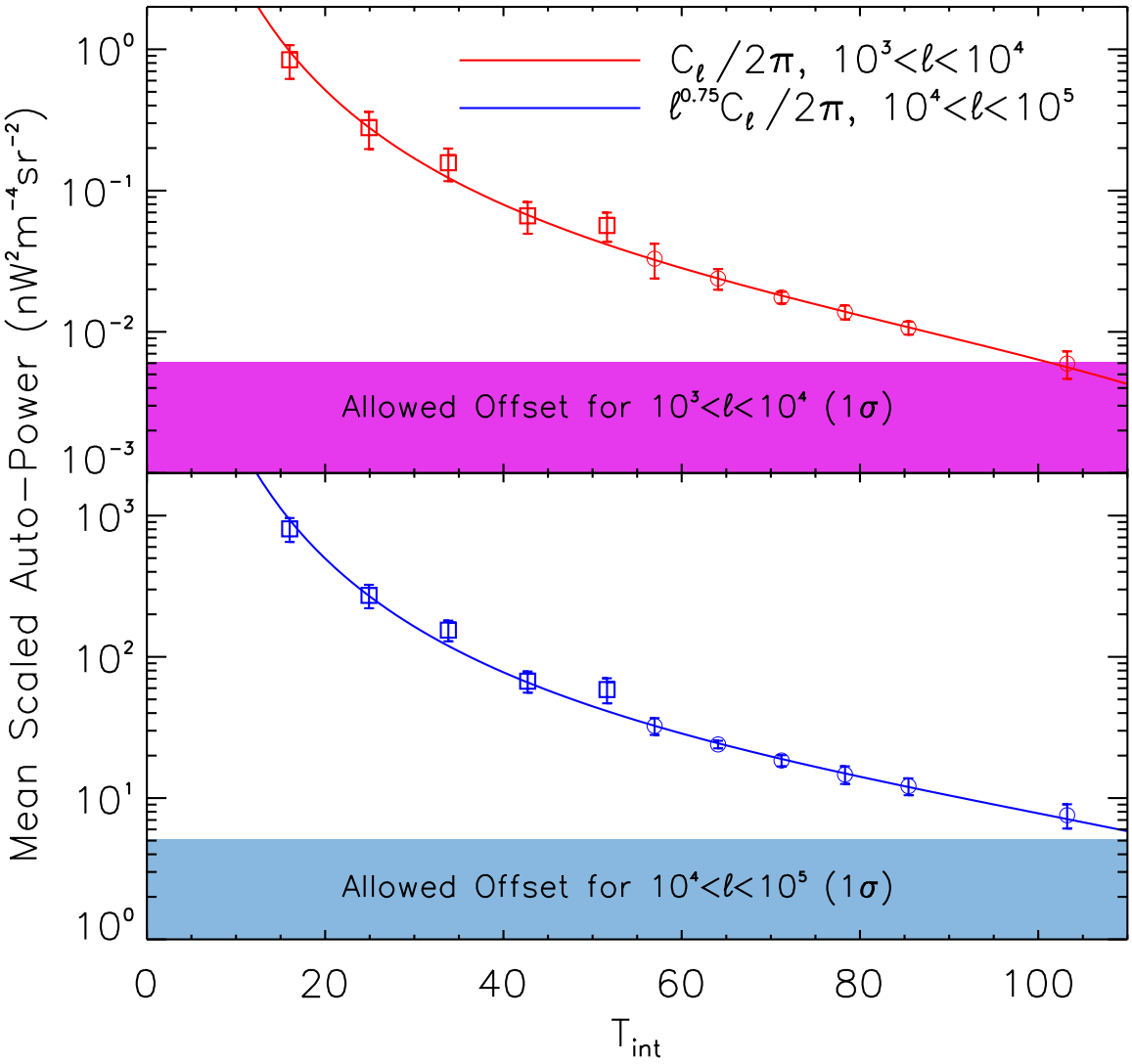

Fig. 14.— Scaled noise power versus integration time for the LAMP field-difference data. The upper plot shows the mean power at each value of $T_{\rm int}$ for the $10^3 < \ell < 10^4$ bandpower averages, and the lower panel the same for $10^4 < \ell < 10^5$. The lines indicate the best fitting model of the form $C_\ell = a_{\rm read}T^{-3} + a_{\rm photon}T^{-1} + a_{\rm sky}$ in both cases. Finally, the colored regions show the allowed 1σ uncertainty $a_{\rm off}$ from the fit, which we use to place constraints on the amplitude of noise which arises from a hypothetical component associate with emission from the sky.

the two ℓ ranges equivalent to the upper limits plotted in Figure 12. As these reflect systematic uncertainties due to various corrections in the data pipeline we cannot add them to the overall uncertainty in the limit, but based on the amplitude of the changes in the noise limits we can infer that these systematic errors make at most a 5 % change in the upper limit we quote. Similar analyses with larger data sets will require care with these type of systematics, but they do not limit our understanding of the data in this study.

Table 5: Systematic uncertainties and their effect on power spectral noise upper limits.

Systematic	Estimate	$\ell(\ell+1)\langle\delta C_{\ell,\mathrm{sky}}\rangle/2\pi$ (nW m^{-2} sr^{-1})	
Error		$10^3 < \ell < 10^4$ ($\times 10^{-2}$)	$10^4 < \ell < 10^5$ ($\times 10^{-4}$)
Fiducial	-	3.09	1.74
Flat Field	No flat field correction	3.02	1.83
Dark current	Dark current correction -1σ	3.02	1.73
$''$	Dark current correction $+1\sigma$	3.01	1.73

6. Discussion

To the limit we are able to probe with these data, variations in the inter-line continuum level at 1191.3 nm do not appear to be causing a deviation from normal integration-time noise scalings for this detector. Though the total integration time on the sky of 3.5 hrs is not sufficient to approach the diffuse astronomical emission, this result lends confidence to the plausibility of performing narrow-band imaging measurements in the near IR. Sullivan & Simcoe (2012) investigate the possible sources of the terrestrial continuum background near 1.2 μm, and are unable to identify the source of the inter-line continuum, finding it to be larger than the sum of known contributions at these (namely the Lorentzian wings of the OH lines and Zodiacal light). Our results, from an observation site and instrument with significantly different characteristics, are remarkably consistent with those of Sullivan & Simcoe (2012) and suggest that their measurement of the continuum level is correct. Because the source of the inter-line continuum remains a mystery, it is dangerous to speculate whether these observations would eventually become limited by the background continuum. A lower limit to the temporal variability can be set using the model of Sullivan & Simcoe (2012) which gives an OH-wing background of ~ 500 nW m^{-2} sr^{-1} at 1191.3 nm. Assuming 10 % variation in amplitude, the expected noise level from the OH-wings is ~ 1.5 orders of magnitude below our current sensitivity, so it is not clear whether this component would present a fundamental limit to measurements of the near IR background.

Another open issue is the time scale of the emission, which is known to vary on the time scale of minutes (Taylor et al. 1991, Ramsay et al. 1992). Broad-band measurements of airglow in $H-$band show a temporal powers spectrum rising as $1/f$ with a knee at ~ 5 mHz[14]. Because our

[14]Measured by the 2MASS Wide-Field Airglow Experiment, http://www.astro.virginia.edu/ mfs4n/2mass/airglow/adams/syp.ps.

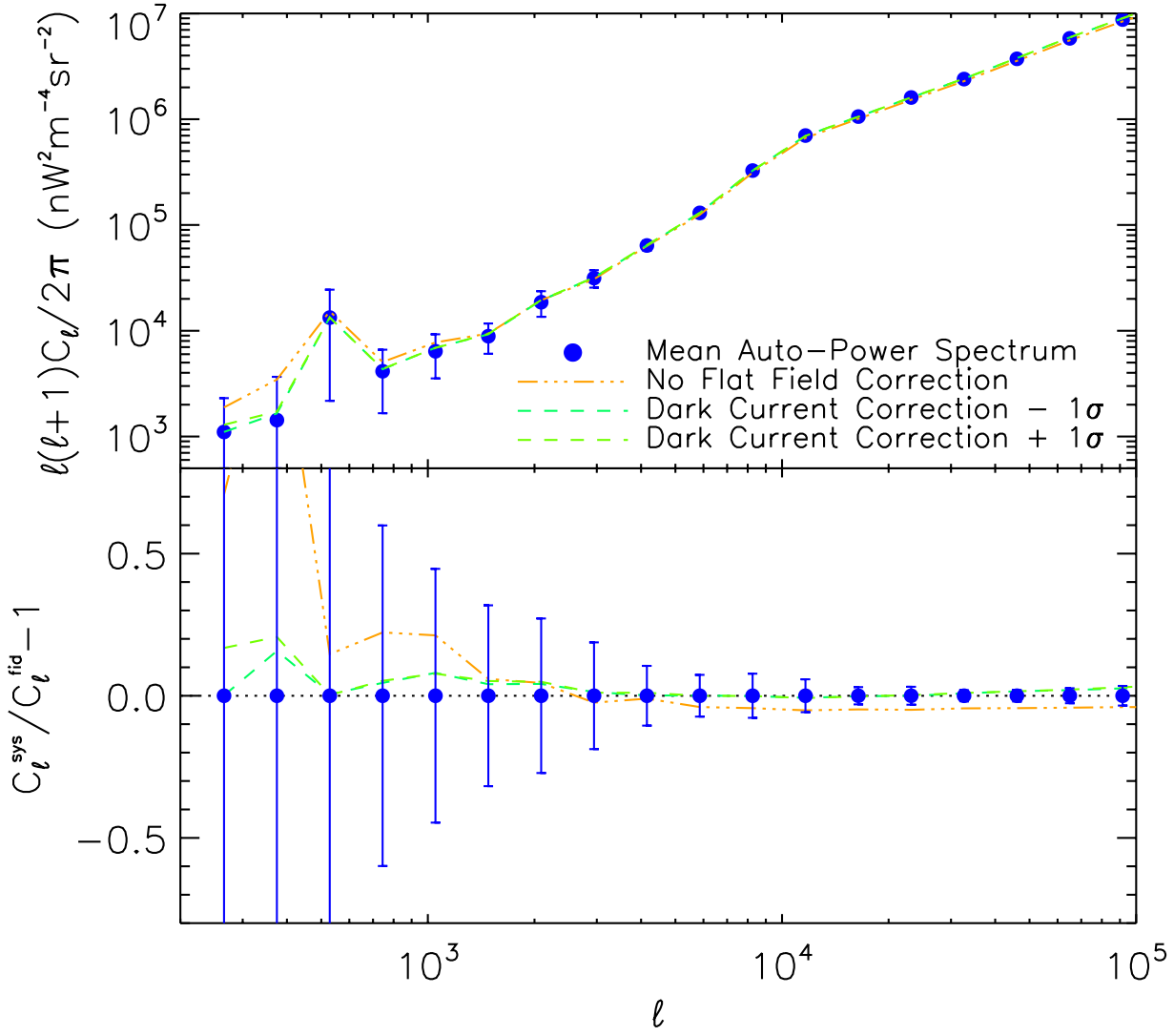

Fig. 15.— Sources of systematic errors and limits on their effect on the mean auto-power spectrum. To investigate the effect of the two major systematic uncertainties in this study, namely the flat field responsivity correction and the dark current subtraction, we compute the auto-power spectra in the fiducial case (points), and then (i) with no flat field correction applied; (ii) with the dark current subtraction under-estimated by the overall variance in the set; and (iii) with the dark current subtraction over-estimated by the overall variance in the set. The upper panel shows power spectra scaled by $\ell(\ell+1)/2\pi$ which can be compared directly to Figure 12. The lower panel shows the ratio between the fiducial power spectrum and the systematic test of interest. The flat field systematic has the largest effect on the measurement, overestimating the power at low-ℓ and slightly underestimating the power at high-ℓ. When propagated to overall uncertainty on the atmospheric noise component, we find at most a 5 % variation from the fiducial upper limit.

spatial power spectra are differences of $\sim 100\,\mathrm{s}$ integrations, we are probing the airglow stability on timescales similar to this. Unlike high-spectral resolution instruments (Sullivan & Simcoe 2012), we are not concerned about time scales longer than a few minutes because it is possible to design an $R \sim 500$ narrow-band imaging instrument to be photon-noise limited in $\sim 100\,\mathrm{s}$.

Though based on a limited data set, these results are encouraging for the general approach of imaging the near IR background through narrow windows in the Meinel emission. With a suitable instrument, observation design, and careful attention to systematics, it seems realistic to achieve the sensitivity required to measure diffuse astronomical emission from the ground.

The authors wish to thank Jaime Luna for his help designing the LAMP mechanical assembly, Heath Rhoades at JPL's Table Mountain Observatory for his assistance setting up the instrument and guidance using the $24''$ telescope, and the Gemini Observatory for making their sky model tables public. The development of LAMP was supported by the JPL Research and Technology Development Fund. This publication makes use of data products from the Two Micron All Sky Survey (2MASS), which is a joint project of the University of Massachusetts and the Infrared Processing and Analysis Center/California Institute of Technology, funded by the National Aeronautics and Space Administration and the National Science Foundation.

REFERENCES

Bock, J., Sullivan, I., Arai, T., et al. 2013, ApJS, 207, 32

Cuby, J. G., Lidman, C., Moutou, C., & Petr, M. 2000, in Society of Photo-Optical Instrumentation Engineers (SPIE) Conference Series, Vol. 4008, Optical and IR Telescope Instrumentation and Detectors, ed. M. Iye & A. F. Moorwood, 1036–1047

Ellis, S. C., Bland-Hawthorn, J., Lawrence, J., et al. 2012, MNRAS, 425, 1682

Garnett, J. D., & Forrest, W. J. 1993, in Society of Photo-Optical Instrumentation Engineers (SPIE) Conference Series, Vol. 1946, Infrared Detectors and Instrumentation, ed. A. M. Fowler, 395–404

Helgason, K., Ricotti, M., & Kashlinsky, A. 2012, ApJ, 752, 113

Hivon, E., Górski, K. M., Netterfield, C. B., et al. 2002, ApJ, 567, 2

Kashlinsky, A., Arendt, R. G., Mather, J., & Moseley, S. H. 2005, Nature, 438, 45

Kelsall, T., Weiland, J. L., Franz, B. A., et al. 1998, ApJ, 508, 44

Knox, L. 1995, Phys. Rev. D, 52, 4307

Korngut, P. M., Renbarger, T., Arai, T., et al. 2013, ApJS, 207, 34

Lang, D., Hogg, D. W., Mierle, K., Blanton, M., & Roweis, S. 2010, AJ, 139, 1782

Le Texier, H., Solomon, S., & Garcia, R. R. 1987, Planet. Space Sci., 35, 977

Leblanc, T., Walsh, T. D., McDermid, I. S., et al. 2011, Atmospheric Measurement Techniques, 4, 2579

Leinert, C., Bowyer, S., Haikala, L. K., et al. 1998, A&AS, 127, 1

Lord, S. D. 1992, A new software tool for computing Earth's atmospheric transmission of near- and far-infrared radiation, Tech. rep.

Maihara, T., Iwamuro, F., Yamashita, T., et al. 1993, PASP, 105, 940

Matsumoto, T., Seo, H. J., Jeong, W.-S., et al. 2011, ApJ, 742, 124

Meinel, I. A. B. 1950, ApJ, 111, 555

Ramsay, S. K., Mountain, C. M., & Geballe, T. R. 1992, MNRAS, 259, 751

Skrutskie, M. F., Cutri, R. M., Stiening, R., et al. 2006, AJ, 131, 1163

Sullivan, P. W., & Simcoe, R. A. 2012, PASP, 124, 1336

Taylor, M. J., Turnbull, D. N., & Lowe, R. P. 1991, Geophys. Res. Lett., 18, 1349

von Savigny, C., McDade, I. C., Eichmann, K.-U., & Burrows, J. P. 2012, Atmospheric Chemistry & Physics, 12, 8813

Zemcov, M., Arai, T., Battle, J., et al. 2013a, ApJS, 207, 31

—. 2013b, ApJS, 207, 31